NASA/TM–20260003187

A Study of Space Environment Effect on Highly Thermally Conductive Hybrid Carbon Fiber Polymer Composites

Joy Rosado
OSTEM Internship Program, Langley Research Center, Hampton, Virginia

Jin Ho Kang
NASA Langley Research Center, Hampton, Virginia

Keith L. Gordon
NASA Langley Research Center, Hampton, Virginia

Grace Belancik
NASA Ames Research Center, Mountain View, California

Pranav Jagtap
Amentum / NASA Ames Research Center, Mountain View, California

April 2026

NASA STI Program Report Series

Since its founding, NASA has been dedicated to the advancement of aeronautics and space science. The NASA scientific and technical information (STI) program plays a key part in helping NASA maintain this important role.

The NASA STI program operates under the auspices of the Agency Chief Information Officer. It collects, organizes, provides for archiving, and disseminates NASA's STI. The NASA STI program provides access to the NTRS Registered and its public interface, the NASA Technical Reports Server, thus providing one of the largest collections of aeronautical and space science STI in the world. Results are published in both non-NASA channels and by NASA in the NASA STI Report Series, which includes the following report types:

- TECHNICAL PUBLICATION. Reports of completed research or a major significant phase of research that present the results of NASA Programs and include extensive data or theoretical analysis. Includes compilations of significant scientific and technical data and information deemed to be of continuing reference value. NASA counterpart of peer-reviewed formal professional papers but has less stringent limitations on manuscript length and extent of graphic presentations.

- TECHNICAL MEMORANDUM. Scientific and technical findings that are preliminary or of specialized interest, e.g., quick release reports, working papers, and bibliographies that contain minimal annotation. Does not contain extensive analysis.

- CONTRACTOR REPORT. Scientific and technical findings by NASA-sponsored contractors and grantees.

- CONFERENCE PUBLICATION. Collected papers from scientific and technical conferences, symposia, seminars, or other meetings sponsored or co-sponsored by NASA.

- SPECIAL PUBLICATION. Scientific, technical, or historical information from NASA programs, projects, and missions, often concerned with subjects having substantial public interest.

- TECHNICAL TRANSLATION. English-language translations of foreign scientific and technical material pertinent to NASA's mission.

Specialized services also include organizing and publishing research results, distributing specialized research announcements and feeds, providing information desk and personal search support, and enabling data exchange services.

For more information about the NASA STI program, see the following:

- Access the NASA STI program home page at http://www.sti.nasa.gov

- Help desk contact information:

https://www.sti.nasa.gov/sti-contact-form/
and select the "General" help request type.

NASA/TM–20260003187

A Study of Space Environment Effect on Highly Thermally Conductive Hybrid Carbon Fiber Polymer Composites

Joy Rosado
OSTEM Internship Program, Langley Research Center, Hampton, Virginia

Jin Ho Kang
NASA Langley Research Center, Hampton, Virginia

Keith L. Gordon
NASA Langley Research Center, Hampton, Virginia

Grace Belancik
NASA Ames Research Center, Mountain View, California

Pranav Jagtap
Amentum / NASA Ames Research Center, Mountain View, California

National Aeronautics and
Space Administration

Langley Research Center
Hampton, Virginia 23681-2199

April 2026

National Aeronautics and
Space Administration

Langley Research Center
Hampton, Virginia 23681-2199

April 2026

Available from:

NASA STI Program / Mail Stop 050
NASA Langley Research Center
Hampton, VA 23681-2199

Abstract

A set of novel highly thermally conductive hybrid carbon fiber (CF) polymer composites has been developed for lightweight thermal radiator applications in space missions. This study investigates the effects of the space environment on these materials following exposure in low-Earth orbit (LEO) during the Materials International Space Station Experiment (MISSE)-17 flight mission, where samples experienced 159 days of combined atomic oxygen (AO), ultraviolet (UV) radiation, high vacuum, space radiation and thermal cycling. Post-flight characterization included weight loss, surface morphology, thermo-optical properties, molecular structures, glass transition temperature, thermal degradation and thermal conductivity analyses. The pyrolytic graphite sheet (PGS) samples exhibited negligible weight loss, stable thermo-optical property, and only minor oxidation signature on the exposed surface. Although AO erosion of the epoxy polymer matrix was evident, carbon nanotube (CNT)-infused PGS/CF epoxy composites retained high thermal emissivity and preserved their high thermal conductivities. These results demonstrate that the novel highly thermally conductive hybrid CF composites possess strong environmental resilience and are promising candidates for lightweight thermal radiators and thermal management components in future space exploration missions.

1. Introduction

Materials deployed in space are exposed to a combination of extreme environmental conditions, including ultraviolet (UV) radiation, high vacuum, ionizing space radiation and large temperatures fluctuations. These conditions can significantly alter material properties and contribute to long-term degradation. Previous studies from the Materials International Space Station Experiment (MISSE) missions have demonstrated that materials in low Earth orbit (LEO) experience substantial degradation under these conditions, particularly due to the additional corrosive effects of atomic oxygen (AO) [1-2].

This study investigates the effects of the space environment on newly developed materials intended for use in a novel composite thermal radiator-based CO_2 deposition (CDep) removal system, designed for high-performance atmospheric revitalization [3]. The CDep system exploits the differences in condensation and deposition temperatures among atmospheric constituents to selectively remove carbon dioxide from air streams [6]. The work focuses on hybrid carbon fiber (CF) composite materials including pyrolytic graphite sheets (PGS) and PGS/CF polymer composites. By comparing the behavior and properties of these materials exposed to the harsh environment of space during the MISSE-17 flight mission with those of unexposed control samples, this study identifies the material property changes induced by the exposure to the LEO environment. Post-flight analyses include weight loss, surface morphology, thermo-optical properties, molecular structures, glass transition temperature, thermal degradation and thermal conductivity analyses.

2. Experimental

2.1 MISSE-17 Mission

Space environment exposure testing was performed as part of the MISSE-17 flight mission. MISSE-17 was launched aboard Space X CRS-27 to the International Space Station (ISS) on March 14, 2023, carrying four MISSE Science Carriers (MSCs), which included ten samples used in this study. The MSCs were installed on the MISSE Flight Facility (MISSE-FF)

on March 27, 2023, with the samples positioned on the zenith-facing side of the MISSE-FF. Sample exposure to the space environment began on April 5, 2023, when the MSCs were first opened, with several subsequent closures occurring as required to support ISS operations. The final closure occurred on September 14, 2023. The total exposure duration for the zenith-facing sample was 159 days 2 hours, and 22 minutes. MISSE-17 returned to Earth aboard Space X CRS-29 on December 22, 2023.

2.2 Materials

A total of sixteen samples were analyzed in this study, consisting of ten samples exposed to the space environment and six control samples maintained under Earth conditions. The materials evaluated included seven PGS samples, and eight PGS/CF epoxy composite samples. PGS films were manufactured by Panasonic Industry (Japan). Novolac epoxy (PMT F7, Patz Materials, U.S.) resin and polyacrylonitrile (PAN) based spread-tow, carbon fiber (Torayca^{TM} M30S, Toray US, U.S.) fabric were used as base prepreg materials. Detailed material descriptions are available in reference [3]. The PGS samples were arranged in a four-layer stack, each layer having a distinct thickness. The top layer (Z1-1), directly exposed to the space environment, was 25 μm thick. The second layer (Z1-2) was also 25 μm thick, followed by a 70 μm thick layer (Z1-3), and a 100 μm layer at the bottom (Z1-4). Corresponding control samples, named Z1-1-C, Z1-3-C and Z1-4-C were fabricated with matching thicknesses. All PGS samples measured 50.8 mm × 76.2 mm. Table 1 summarizes the PGS samples and their respective exposure conditions.

Table 1. PGS sample configurations and corresponding exposure conditions.

MISSE Sample ID (in MISSE-17)	Sample ID (in the study)	Description	Sample Condition
M17-GK-Z1-1	Z1-1	GS-25 [PGS, thickness 25 μm]	Exposed – First Layer
M17-GK-Z1-2	Z1-2	GS-25 [PGS, thickness 25 μm]	Exposed – Second Layer
M17-GK-Z1-3	Z1-3	GS-70 [PGS, thickness 70 μm]	Exposed – Third Layer
M17-GK-Z1-4	Z1-4	GS-100 [PGS, thickness 100 μm]	Exposed – Fourth Layer
M17-GK-Z1-1-C	Z1-1-C	GS-25 [PGS, thickness 25 μm]	Control

M17-GK-Z1-3-C	Z1-3-C	GS-70 [PGS, thickness 70 μm]	Control
M17-GK-Z1-4-C	Z1-4-C	GS-100 [PGS, thickness 100 μm]	Control

In addition to the PGS samples, composite samples were also evaluated. These composites included two PGS/CF epoxy composites, arranged in a two-layer stack with sample Z2-1 positioned above Z2-2. Two carbon nanotube (CNT) infused PGS/CF epoxy composites, consisting of PGS 25 μm, CF and epoxy matrix, were similarly stacked with sample Z3-1 placed above Z3-2. Finally, two CNT infused PGS/CF epoxy composites samples, consisting of PGS 70 μm, PGS and epoxy matrix, were also stacked with sample Z4-1 placed above Z4-2. Corresponding control samples, maintained under Earth conditions, were included to provide a baseline for assessing property changes induced by space exposure. Table 2 summarizes the composite sample configurations and their respective exposure conditions.

Table 2. Composite sample configurations and corresponding exposure conditions.

Sample ID	Description	Material Composition	Sample Condition
Z2-1	CF-PMT F7/ perforated PGS 25 / CF-PMT F7	CF, PGS 25, Epoxy Composite	Exposed – First Layer
Z2-2			Exposed – Second Layer
Z2-C			Control
Z3-1	CNT2% CF-PMT F7/ perforated PGS 25 / CNT2% CF-PMT F7	CNT/CF, PGS 25, Epoxy Composite	Exposed – First Layer
Z3-2			Exposed – Second Layer
Z3-C			Control
Z4-1	CNT2% CF-PMT F7/ perforated PGS 70 / CNT2% CF-PMT F7	CNT/CF, PGS 70, Epoxy Composite	Exposed – First Layer
Z4-2			Exposed – Second Layer
Z4-C			Control

2.3 Characterization

Material property characterization was performed to evaluate the effects of the space-exposure on samples. Dry weight measurement was obtained using an analytical balance (Excellence Plus XP, Mettler Toledo) after drying the samples at approximately 100°C under vacuum for 24 hours. Morphological characterization was performed using an optical microscope (DM800 with DFC450 digital camera, Leica) and an optical profilometer (MicroProf

100 profilometer, FRT). The thermo-optical properties were measured using a portable emissometer (TEMP 2000, AZ Technology) over a wavelength range (λ) of 3 μm to 30 μm and a ultraviolet/visible/near-infrared (UV/VIS/NIR) spectrometer (Lambda 1050 UV/VIS/NIR spectrometer, Perkin Elmer) over a wavelength range of 250 nm to 2500 nm. Molecular structure of materials was assessed using Fourier-transform infrared (FT-IR) spectroscopy (Nicolet™ i5™ FTIR, Thermo Scientific) over a wavenumber range of 400 cm^{-1} to 4000 cm^{-1}. The glass transition temperature was determined using a modulated differential scanning calorimeter (DSC 25, TA Instruments) at a heating rate of 3°C/min with a modulation of ±0.47°C for every 60 seconds. Thermal degradation behavior was evaluated using a thermogravimetric analyzer (TGA 50, TA instrument) at a heating rate of 10°C/min under both air and nitrogen atmosphere atmospheres. Thermal conductivity under ambient conditions was measured using a hot disk thermal constants analyzer (TPS 2500S, Hot Disk AB) equipped with sensors (model 5465, 5501, 7280, 7577 and 102003). In this technique, the sensor is placed between two pieces of the sample and functions simultaneously as a heat source and a dynamic temperature detector. Multiple samples and/or measurement locations were evaluated to ensure the reliability of the data.

3. Results and Discussion

3.1 Weight Loss

The weight of each sample was measured before and after exposure to the space environment to quantify material loss resulting from erosion or other degradation mechanisms. Comparison of pre-flight and post-flight weights enables calculation of weight differences and percent weight loss for each specimen, as summarized in Table 3. The balance repeatability is 0.01mg. However, for conservative data reliability, any change smaller than 0.1mg was considered negligible. The results indicate that samples directly exposed to the space environment (first-layer samples) exhibited the highest percentages of weight loss (e.g., Z2-1 vs Z2-2 or Z3-1 vs Z3-2). The first-layer PGS/CF epoxy composite (Z2-1) experienced approximately 0.5 wt.% weight loss, whereas the PGS sample (Z1) exhibited no significant weight change, demonstrating the resilience of the graphene-based structure relative to the epoxy

matrix composite when exposed to atomic oxygen (AO), UV and space radiation. Interestingly, CNT-infused PGS/CF epoxy composites (Z3-1, Z4-1) exhibited slightly higher weight loss of approximately 0.7 wt.%. Notably, even their second layers (Z3-3, Z4-2) exhibited substantial weight loss of approximately 0.25–0.27 wt.%, compared with approximately 0.15 wt.% for the second-layer PGS/CF epoxy composite without CNT (Z2-2) infusion. This behavior may result from the outgassing of low molecular weight fragments or unreacted monomers within epoxy resin system. The tubular CNT network in epoxy resin may exacerbate this effect by providing pathways that facilitate the escape of volatile species in high vacuum environment of low Earth orbit.

Table 3. Pre-Flight and Post-Flight Mass Comparison of Samples.

Sample	Pre-Flight (g)	Post-Flight (g)	Mass difference (g)	Percentage (%)
Z1-1	0.1789	0.1787	**-0.00020**	**-0.11**
Z1-2	0.17831	0.17834	0.00003 (negligible)	0.02 (negligible)
Z1-3	0.31883	0.31882	-0.00001 (negligible)	0.00 (negligible)
Z1-4	0.32176	0.3218	0.00004 (negligible)	0.01 (negligible)
Z1-1-C	0.17938	0.17941	0.00003 (negligible)	0.02 (negligible)
Z1-3-C	0.31778	0.31774	-0.00004 (negligible)	-0.01 (negligible)
Z1-4-C	0.32578	0.32582	0.00004 (negligible)	0.01 (negligible)
Z2-1	0.77473	0.77069	**-0.00404**	**-0.52**
Z2-2	0.75706	0.75596	-0.00110	-0.15
Z3-1	0.90688	0.90054	**-0.00634**	**-0.70**
Z3-2	0.98546	0.98302	-0.00244	-0.25
Z4-1	1.18052	1.17223	**-0.00829**	**-0.70**
Z4-2	1.28974	1.2862	-0.00354	-0.27

3.2 Photographs and Optical Microscopy

Photographs were taken for all the post-flight samples and the pre-flight control samples to visually evaluate the effects of space exposure. These images were examined for evidence of erosion, discoloration, surface degradation or other form of damage incurred during the MISSE-

17 mission. Visual inspection was complemented by optical microscopy (OM) to identify microscopic changes in surface morphology and other features influences by the LEO environment. A prominent observation was the distinct color change on surfaces directly exposed to space, which developed a yellowish hue (e.g., Z1-1 front vs Z1-1 back in Figure 1, and Z2-1 front vs Z2-1 back in Figure 2).

For the PGS samples, this yellowish coloration is likely attributed to oxidation and the formation of graphite oxide. In the composite samples, the observed color change may result from degradation, oxidation or molecular-level alterations within the epoxy matrix due to exposure to UV radiation and AO. Figures 1–4 illustrate the visible and microscopic effects of space exposure, highlighting changes in coloration, surface morphology or other differences between exposed and control samples.

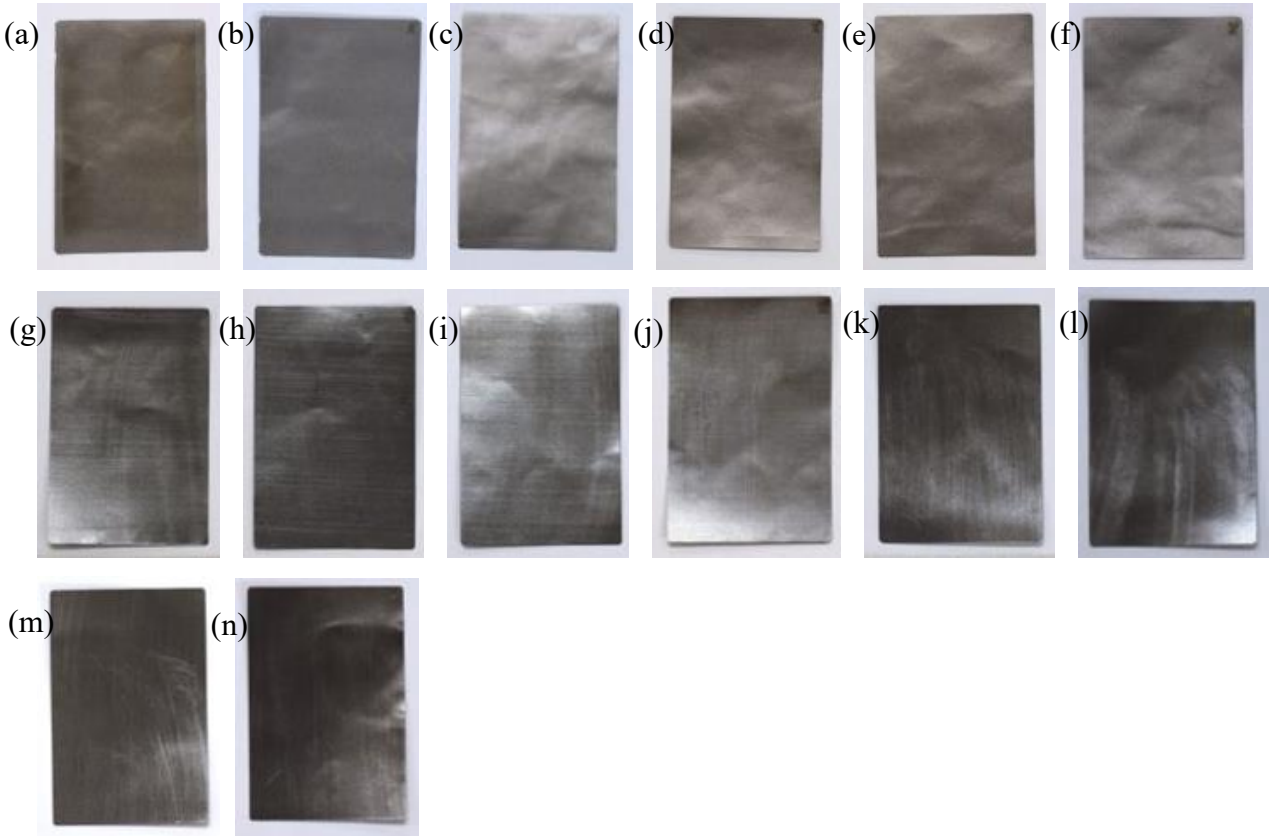

Figure 1. Photographs of PGS samples (a) Z1-1 front, (b) Z1-1 back, (c) Z1-2 front, (d) Z1-2 back, (e) Z1-1-C front, (f) Z1-1-C back, (g) Z1-3 front, (h) Z1-3 back, (i) Z1-3-C front, (j) Z1-3-C back, (k) Z1-4 front, (l) Z1-4 back, (m) Z1-4-C front, and (n) Z1-4-C back.

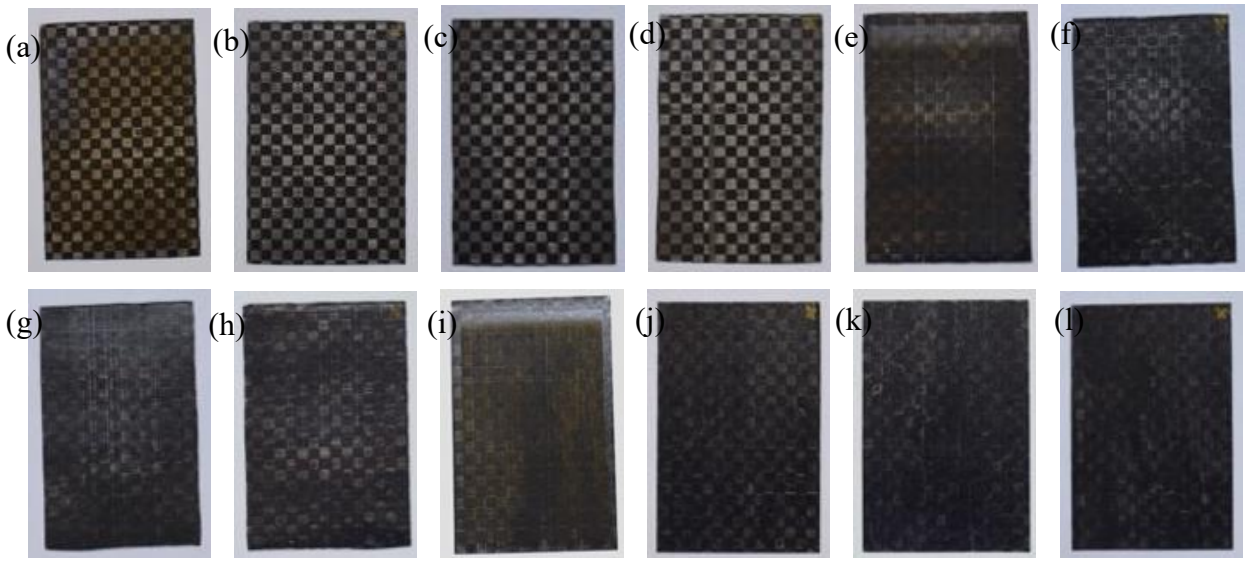

Figure 2. Photographs of composite samples (a) Z2-1 front, (b) Z2-1 back, (c) Z2-2 front, (d) Z2-2 back, (e) Z3-1 front, (f) Z3-1 back, (g) Z3-2 front, (h) Z3-2 back, (i) Z4-1 front, (j) Z4-1 back, (k) Z4-2 front, (l) Z4-2 back.

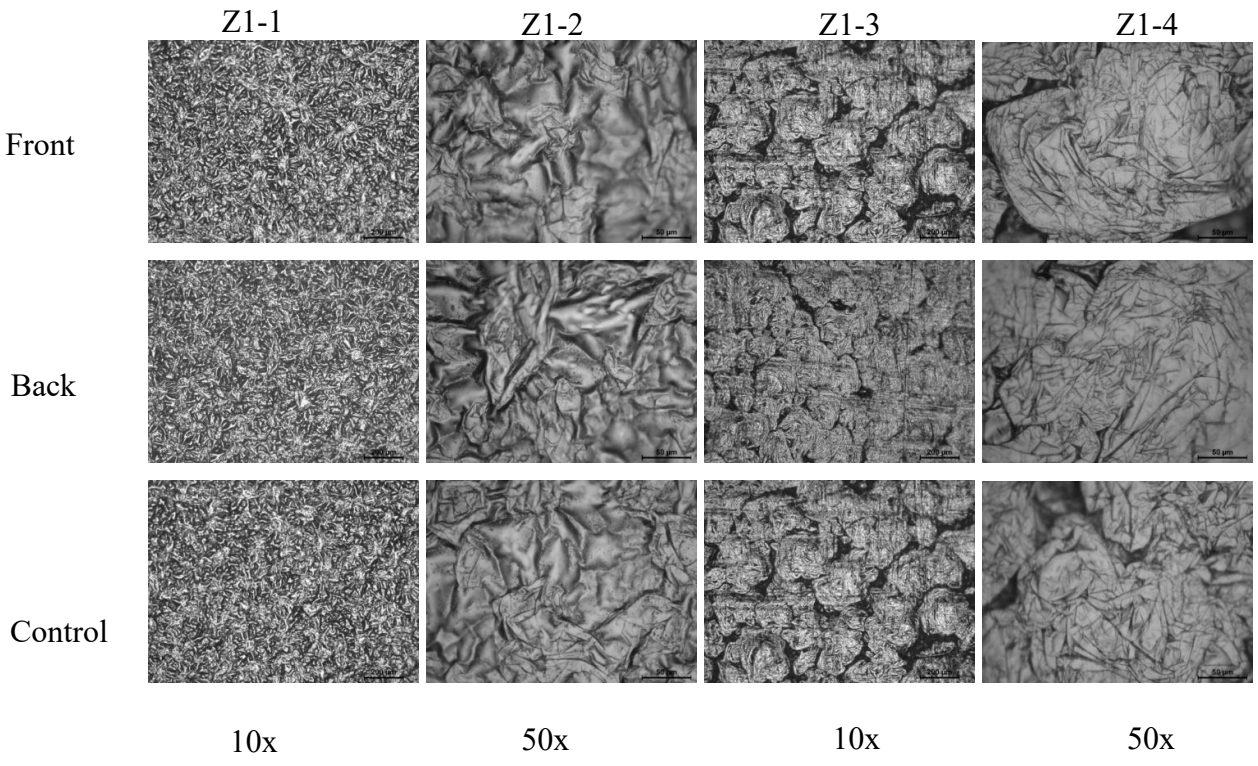

Figure 3. OM images of PGS samples.

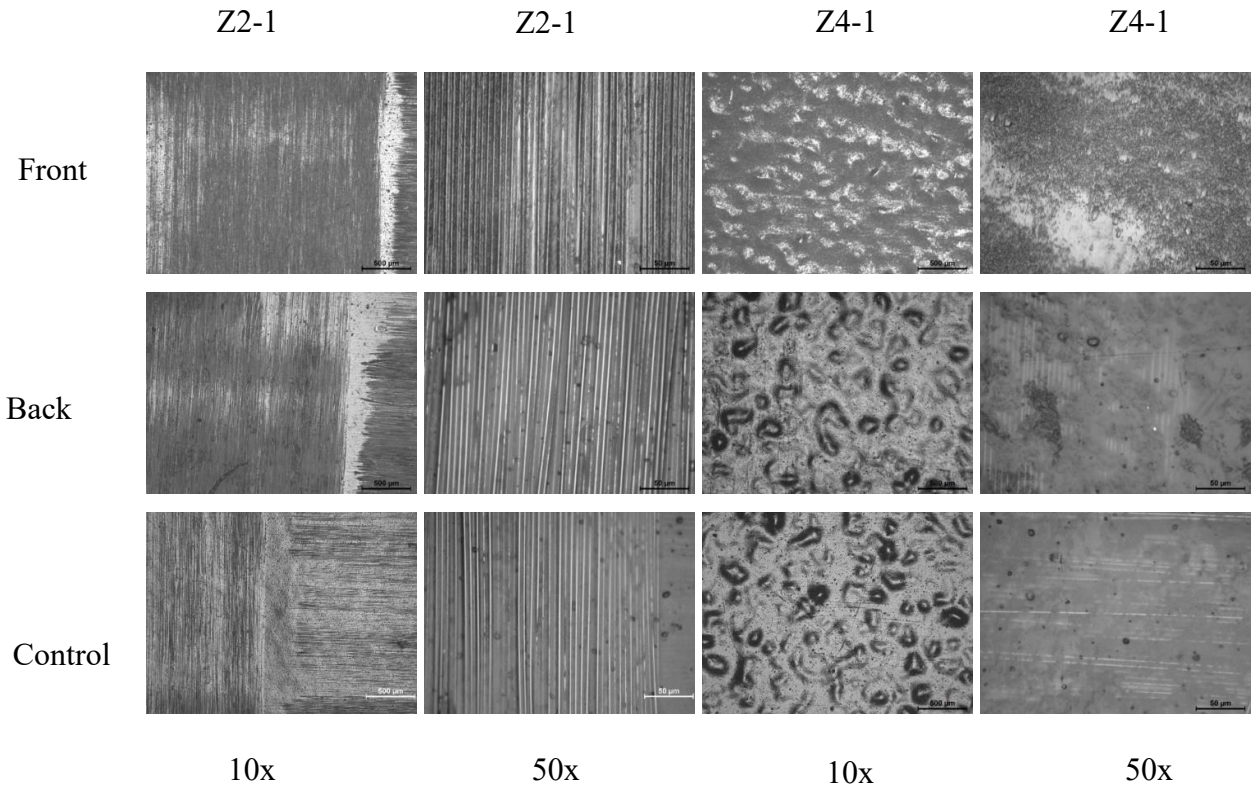

Figure 4. OM images of composite samples.

The OM images provide a detailed comparison between pre-flight control and post-flight samples, revealing differences that were not apparent in the photographs in Figure 2. These results are shown in Figures 3–4 and Figures S.1–S.3 (in Appendix). The PGS samples exhibited no significant microscopic morphological change when comparing the front and back surfaces of post-flight sample with their corresponding pre-flight controls (e.g., Z1-1 front vs. Z1-1 back vs. Z1-1 control or Z2-1 front vs. Z2-2 back vs. Z2-2 control in Figure 3). In contrast, the PGS/CF epoxy composite samples displayed noticeable erosion on the exposed surface. The epoxy matrix exhibited clear signs of degradation, with exposed and dried CFs visible on the space-facing surface (Z2-1 front, 50x magnification in Figure 4). Meanwhile, the back surface (Z2-1 back) and the pre-flight control (Z2-1 control) retained the expected epoxy-embedded fiber morphology, as shown in Figure 4 (50x magnification). This observation is further supported by optical topography results (Figure S.4–S.9 in Appendix).

The CNT-infused PGS/CF epoxy composite exhibited similar morphological changes. While the back sides of CNT-infused PGS/CF sample (Z4-1 back) exhibited no noticeable differences compared to their corresponding pre-flight control (Z4-1 control), the space-exposed surface (Z4-1 front) displayed clear erosion and surface degradation, as illustrated in Figure 4 (50x magnification). These observations highlight the heightened susceptibility of epoxy matrix and the CNT-infused systems to AO degradation in low Earth orbit.

3.3 Thermal emissivity

The thermal emissivity (ε_T) test was conducted to evaluate the ability of the samples to emit thermal radiation after exposure to the space environment. This assessment involved measuring the reflectance (ρ_T) and transmission (τ_T) at a specific wavelength range and subsequently calculating their thermal emissivity (or absorption) according to the energy conservation and Kirchhoff's law of thermal radiation (equation 1):

$$\varepsilon_T + \rho_T + \tau_T = 1 \quad (1)$$

Thermal emissivity represents a material's effectiveness in emitting thermal radiation, with values ranging from 0 (indicating perfectly reflective or transparent) to 1 (a blackbody). A thermal emissivity of 1 means that the material radiates thermal energy optimally across all frequencies. Table 4 presents the reflectance and thermal emissivity for the PGS samples. As shown in table 4, no significant change was observed between the exposed samples and their control sample, with only minor variations within expected experiment uncertainties, including those arising from sample inhomogeneity. In some cases, the exposed sample exhibited slight increases or decreases in thermal emissivity compared to their control, while in other cases, the values were nearly identical. These small deviations are likely due to the surface inhomogeneity, which can affect reflectance measurements and consequently, the calculated thermal emissivity.

For the composite samples (Table 5), the exposed surface of PGS/CF epoxy composite (Z2-1 front) exhibited a measurable decrease in thermal emissivity, with $\Delta\varepsilon_T$ of approximately 0.05—0.06 compared with the unexposed surface of PGS/CF epoxy composite (Z2-1 back) and the control (Z2 control). This reduction is consistent with the erosion of the epoxy matrix on the

exposure surface, which reveals CFs that more strongly reflect IR radiation, resulting in higher thermal reflectance and correspondingly lower thermal emissivity. CNT infused composite samples exhibited higher emissivity than those without CNTs (ε_T ~ 0.88 for Z4-C vs. ε_T ~ 0.73 for Z2-C). No significant change in thermal emissivity was observed on the exposed surface of CNT-doped PGS/CF epoxy composite (Z4-1 front). Even though surface epoxy resin was eroded, the exposed CNTs can absorb thermal IR radiation energy, maintain emissivity levels and show strong thermo-optical resilience in LEO environment.

Table 4. Thermal reflectance and emissivity of PGS samples.

Sample	Film side	Thermal Reflectance (ρ_R)	Thermal Emissivity (ε_T)
Z1-1	Front	0.69 ± 0.00	0.31 ± 0.00
	Back	0.69 ± 0.00	0.31 ± 0.00
Z1-2	Front	0.69 ± 0.00	0.31 ± 0.00
	Back	0.68 ± 0.00	0.32 ± 0.00
Z1-1-C	Front	0.68 ± 0.00	0.32 ± 0.00
	Back	0.68 ± 0.00	0.32 ± 0.00
Z1-3	Front	0.64 ± 0.00	0.36 ± 0.00
	Back	0.64 ± 0.00	0.36 ± 0.00
Z1-3-C	Front	0.67 ± 0.00	0.33 ± 0.00
	Back	0.64 ± 0.00	0.36 ± 0.00
Z1-4	Front	0.65 ± 0.00	0.35 ± 0.00
	Back	0.66 ± 0.00	0.35 ± 0.00
Z1-4-C	Front	0.65 ± 0.00	0.35 ± 0.00
	Back	0.65 ± 0.00	0.35 ± 0.00

Table 5. Thermal reflectance and emissivity of composite samples.

Sample	Film side average	Thermal Reflectance (ρ_R)	Thermal Emissivity (ε_T)
Z2-1	Front	0.32 ± 0.03	0.68 ± 0.03
	Back	0.26 ± 0.02	0.74 ± 0.02
Z2-2	Front	0.29 ± 0.03	0.71 ± 0.03
	Back	0.27 ± 0.03	0.73± 0.03
Z2-C	Front	0.27 ± 0.00	0.73 ± 0.00
	Back	0.27 ± 0.00	0.73 ± 0.00
Z3-1	Front	0.15 ± 0.02	0.85 ± 0.02
	Back	0.14 ± 0.01	0.86 ± 0.01
Z3-2	Front	0.13 ± 0.01	0.87 ± 0.01
	Back	0.14 ± 0.01	0.86 ± 0.01
Z4-1	Front	0.13 ± 0.01	0.87 ± 0.01
	Back	0.13 ± 0.00	0.87 ± 0.00
Z4-2	Front	0.12 ± 0.00	0.88 ± 0.00
	Back	0.12 ± 0.01	0.88 ± 0.01
Z4-C	Front	0.13 ± 0.00	0.87 ± 0.00
	Back	0.12 ± 0.00	0.88 ± 0.00

3.4 UV/VIS/NIR Spectroscopy

UV/VIS/NIR spectroscopy was used to evaluate the reflectance and absorbance of the samples across the ultraviolet (UV), visible (VIS), and near-infrared (NIR) regions of the optical spectrum, spanning 250–2500 nm and covering approximately 96% of solar emission spectrum [5]. This test provides insights into how the materials interact with solar radiation over this broad wavelength range, enabling assessment of any change induced by exposure to the space environment. Figures S.10–S.12 (in Appendix) present the UV/VIS/NIR spectra of the PGS samples and Table 6 summarizes the corresponding solar reflectance and absorbance values. Consistent with the previously thermal reflectance and emissivity data, all the PGS samples exhibited no significant change in solar reflectance and absorbance, regardless of their exposure condition.

Table 6. Solar Reflectance and Absorbance of PGS Samples.

Sample	Film side	Solar Reflectance (α_R)	Solar Absorbance (α_S)
Z1-1	Front	0.39 ±0.10	0.61 ±0.10
	Back	0.41 ±0.09	0.59 ±0.09
Z1-2	Front	0.42 ±0.09	0.58 ±0.09
	Back	0.41 ±0.09	0.59 ±0.09
Z1-1-C	Front	0.42 ±0.09	0.58 ±0.09
	Back	0.42 ±0.09	0.58 ±0.09
Z1-3	Front	0.38 ±0.08	0.62 ±0.08
	Back	0.41 ±0.09	0.59 ±0.09
Z1-3-C	Front	0.41 ±0.08	0.59 ±0.08
	Back	0.38 ±0.08	0.62 ±0.08
Z1-4	Front	0.38 ±0.08	0.62 ±0.08

	Back	0.40 ±0.08	0.60 ±0.08
Z1-4-C	Front	0.41 ±0.08	0.59 ±0.08
	Back	0.39 ±0.08	0.61 ±0.08

Figures S.13–S.15 (in Appendix) present the UV/VIS/NIR spectra of the composite samples and Table 7 summarizes the corresponding solar reflectance and absorbance values. Among these, the CNT-infused samples (Z3 and Z4) exhibited significantly lower solar reflectance compared to the other composite samples without CNT (Z2) which results in higher absorbance ($\boldsymbol{\alpha_S}$~0.93—0.94 for Z3 or Z4 vs $\boldsymbol{\alpha_S}$~0.87 of Z2). Consistent with the previously thermal reflectance and emissivity data, all the composite samples exhibited no significant change in solar reflectance and absorbance, regardless of their exposure condition, indicating strong thermo-optical resilience in the LEO environment.

Table 7. Solar Reflectance and Absorbance of Composite Samples.

Sample	Film side	Solar Reflectance (α_R)	Solar Absorbance (α_S)
Z2-1	Front	0.14 ±0.04	0.86 ±0.04
	Back	0.15 ±0.03	0.85 ±0.03
Z2-2	Front	0.14 ±0.03	0.86 ±0.03
	Back	0.14 ±0.03	0.86 ±0.03
Z2-C	Front	0.13 ±0.03	0.87 ±0.03
	Back	0.13 ±0.02	0.87 ±0.02
Z3-1	Front	0.06 ±0.01	0.94 ±0.01
	Back	0.07 ±0.01	0.93 ±0.01
Z3-2	Front	0.06 ±0.01	0.94 ±0.01
	Back	0.07 ±0.01	0.93 ±0.01

Z4-1	Front	0.06 ±0.01	0.94 ±0.01
	Back	0.07 ±0.01	0.93 ±0.01
Z4-2	Front	0.06 ±0.01	0.94 ±0.01
	Back	0.07 ±0.01	0.93 ±0.01
Z4-C	Front	0.07 ±0.01	0.93 ±0.01
	Back	0.07 ±0.01	0.93 ±0.01

3.5 FT-IR Spectroscopy

Fourier transform infrared (FT-IR) spectroscopy was used to investigate molecular structure change resulting from exposure to the space environment. The FT-IR spectra of the exposed PGS samples (front and back surfaces of Z1-1, Z1-2) and the corresponding control sample are shown in Figure 5. These spectra identify chemical bond and functional group modifications resulting from the LEO exposure, particularly degradation driven by AO and UV radiation. The front surface of the exposed PGS sample (Z1-1) exhibits more distinct changes compared to its back surface and the control sample, as shown in Figure 5. These differences indicate how the front surface experienced greater degradation due to direct exposure to the AO and UV radiation. A strong C-O-C stretching peak near 1200 cm^{-1} further confirms oxidization of graphene structures on PGS by AO.

Figure 6-7 and Figure S.20 (in Appendix) present the FT-IR spectra of the PGS/CF epoxy composite (Z2-1, front and back) and its control and for the CNT-infused PGS/CF epoxy composite (Z4-1, front and back) and its control, respectively. The exposed front surfaces of the first layer composites (Z2-1 and Z4-1) exhibit weaker absorption peaks corresponding to characteristic epoxy resin structures compared to their back surface and control samples, indicating AO-induced erosion of epoxy resin matrix. Furthermore, the C-H bending vibration of aromatic rings near 570 cm^{-1} is notably weaker on the exposed front surfaces (Z2-1 front and Z4-1 front), signifying degradation of aromatic structures. Exposure to the LEO environment leads to changes in multiple absorption bands, indicating chemical bond scission and oxidation within the epoxy matrix. Over time, these processes can generate new absorption peaks or broaden

existing bands due to the formation of degradation products or changes in molecular architecture. UV radiation also significantly alters the chemistry of aromatic epoxy resins and can compromise their structural integrity, as its photon energy is sufficient to break molecular bonds such as C-C and C-O. AO with its high energy flux, additionally erodes and oxidizes bonds in graphite and most hydrocarbon polymers, changing surface morphology and reducing material thickness [6]. Previous study have shown that graphite surfaces degrade uniformly, whereas in carbon-carbon (C/C) composites, the matrix undergoes more severe degradation than the reinforcing fibers [7].

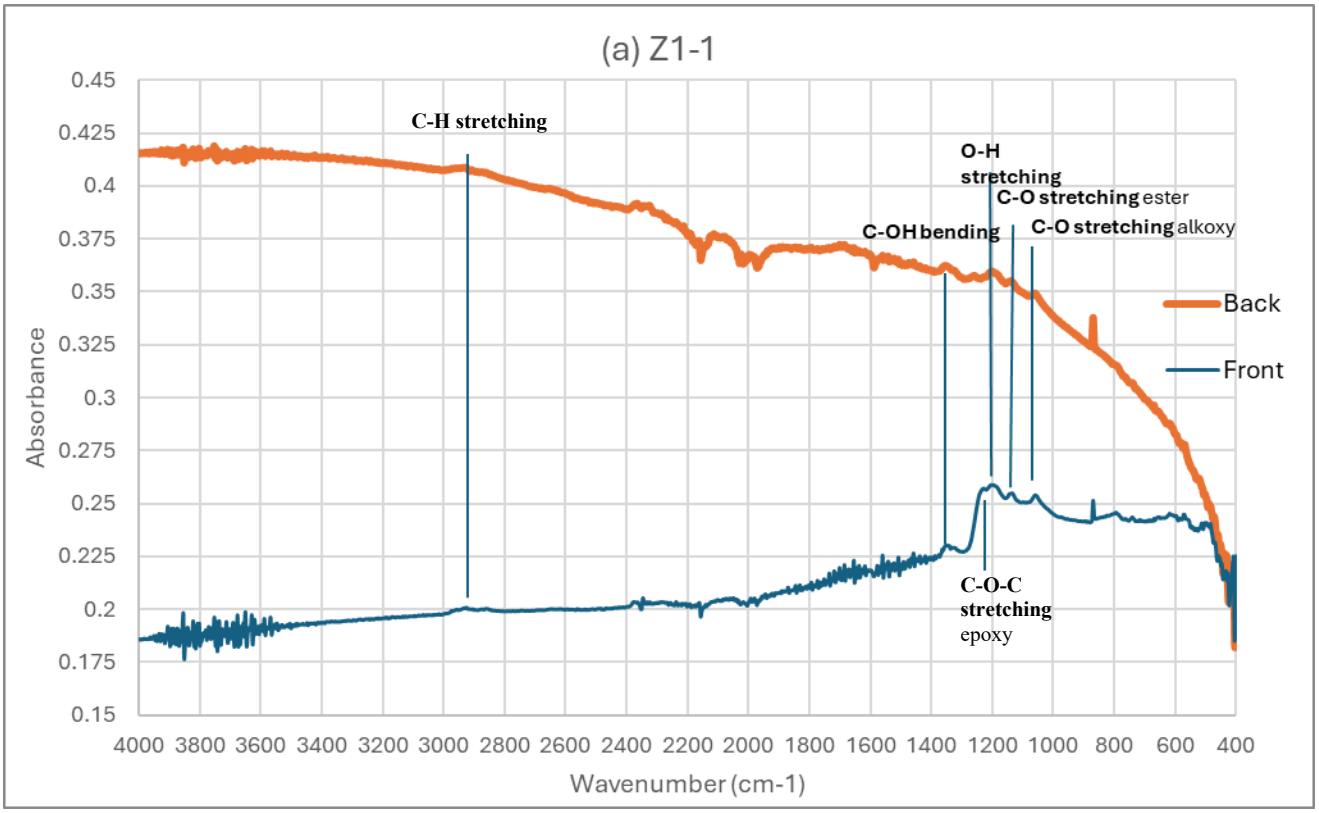

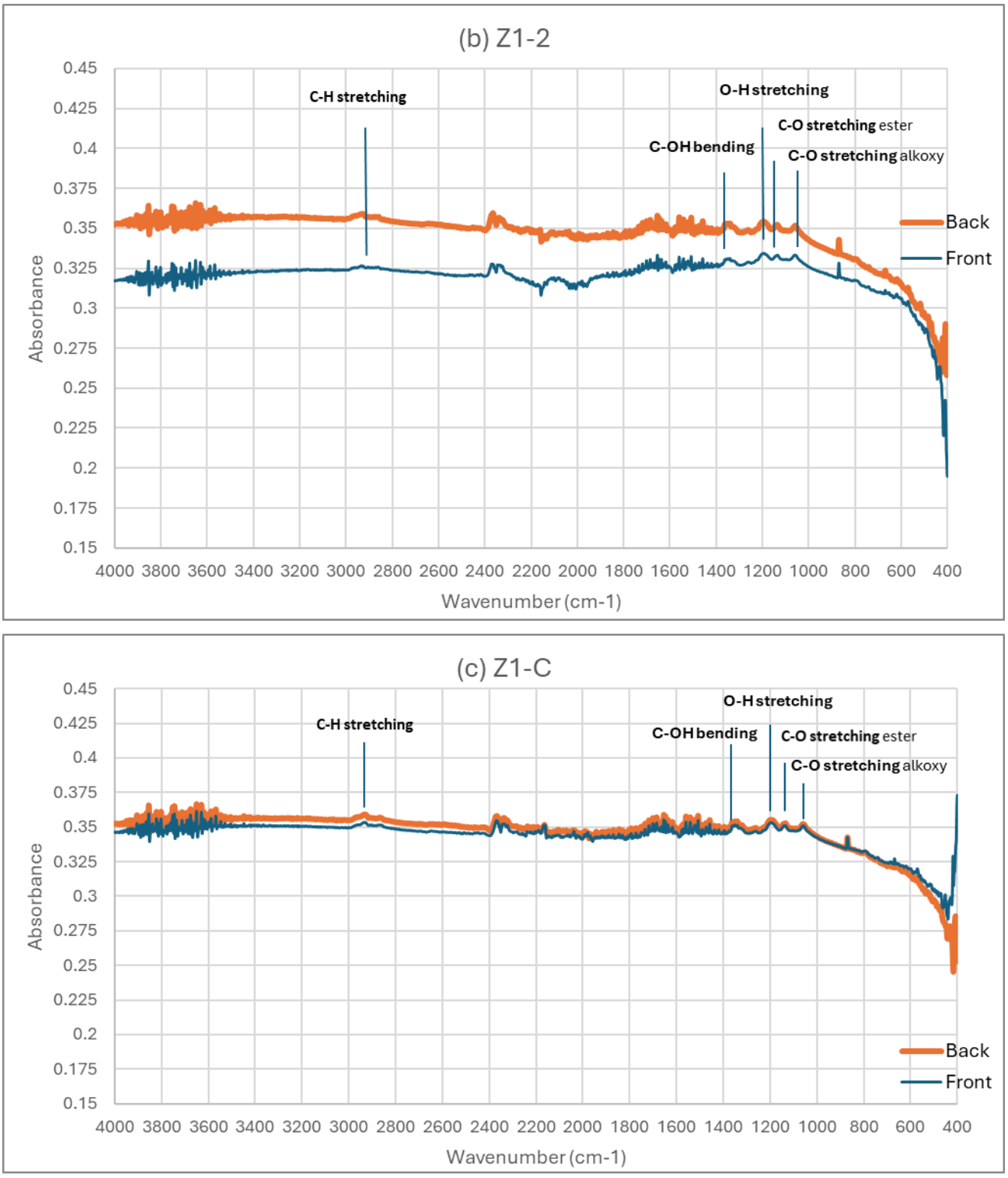

Figure 5. FT-IR spectra of (a) Z1-1, (b) GK-Z1-2, and (c) Z1-C (front and back).

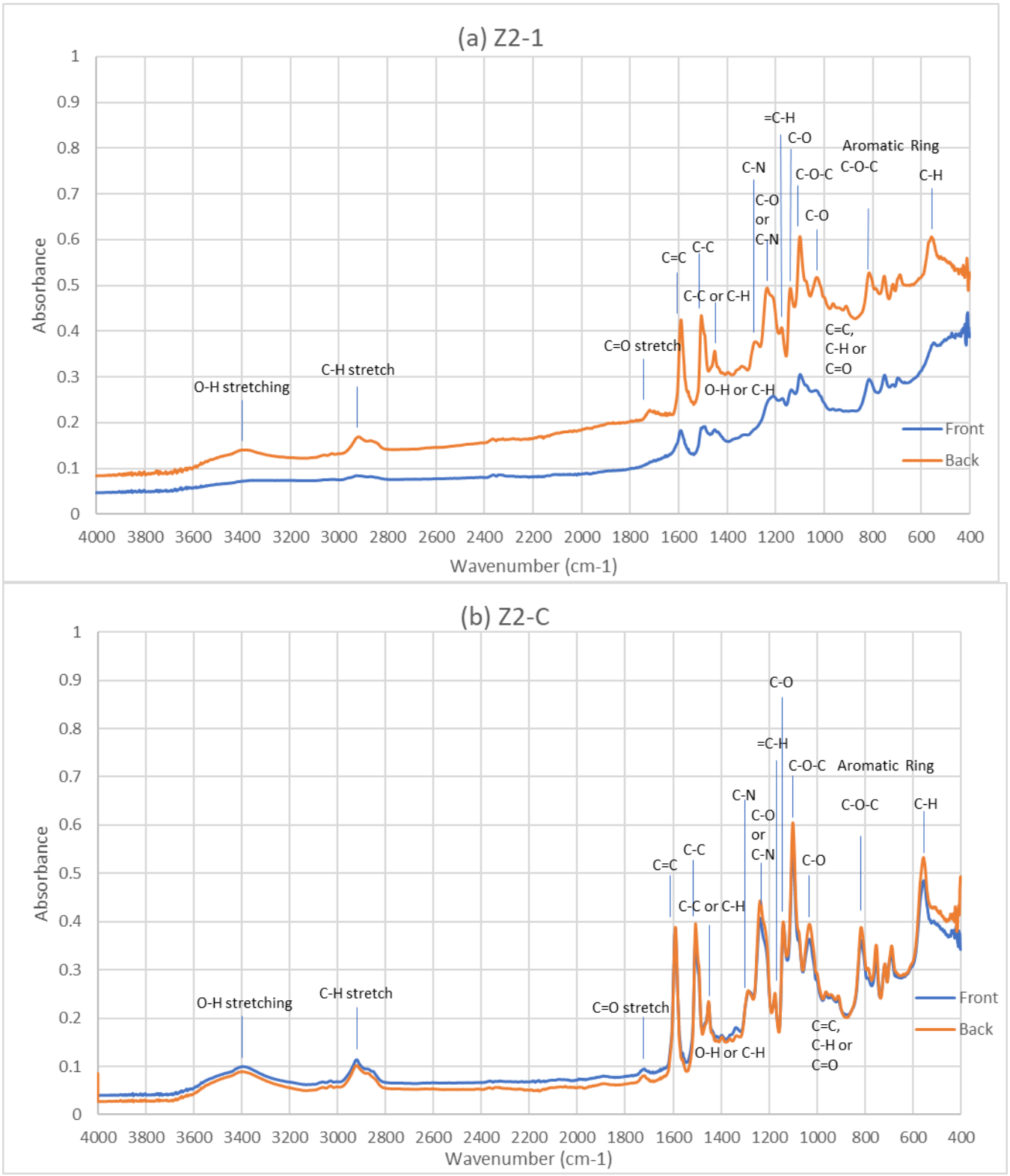

Figure 6. FT-IR spectra of (a) Z2-1 and (b) Z2-C (front and back).

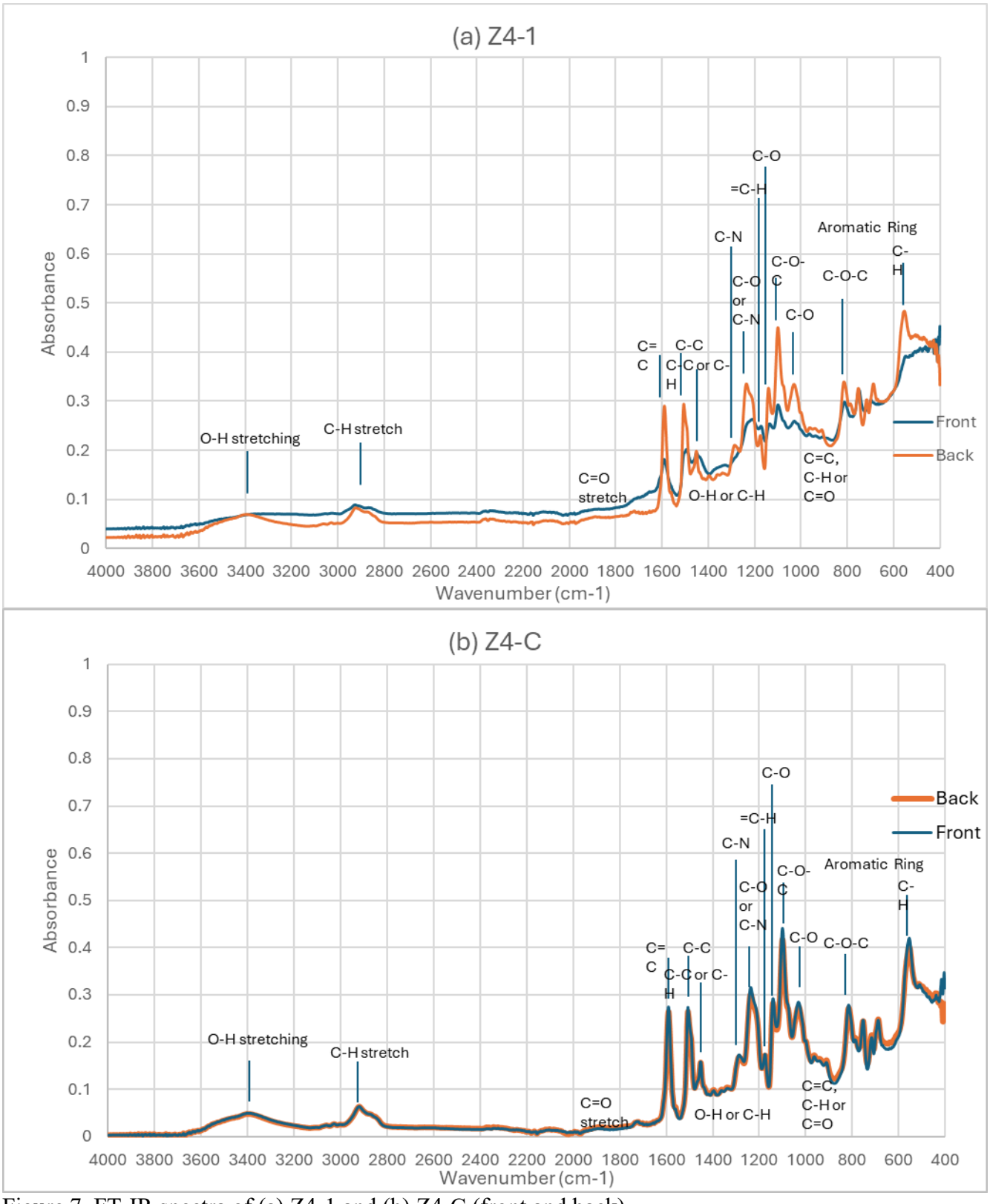

Figure 7. FT-IR spectra of (a) Z4-1 and (b) Z4-C (front and back).

3.6 Thermogravimetric Analysis

Thermogravimetric analysis (TGA) was employed to measure the changes in the mass of a material as a function of temperature. This technique is widely applied for studying decomposition, oxidation, and other thermally activated reactions in materials. By monitoring the magnitude and rate of weight loss under controlled temperature and atmosphere conditions, TGA provides critical insights into thermal stability of materials. In this study, the experiment was conducted under two atmospheric conditions, air and nitrogen, to study the thermal decomposition in both oxidative and inert environments. Key collected data included the weight change of the samples after moisture removal, the temperature corresponding to a 5% weight loss, and the remaining weight percentage at the end of measurement. The resulting thermograms were analyzed using two curves: a green curve representing material's weight change as a function of temperature and a blue curve corresponding to the derivative weight-loss rate.

Figures 8–15 present the TGA results for the PGS samples, showing the weight percentage recorded at every 200°C interval under both air and nitrogen atmospheres. The results indicate that PGS samples exhibited high thermal stability in air up to approximately 700°C. Significant decomposition began near 800°C, followed by a rapid weight loss between 800°C to 985°C, demonstrating a substantial increase in the decomposition rate at elevated temperatures. Under a nitrogen atmosphere, the PGS samples exhibited no meaningful weight loss and maintained thermal stability up to the highest temperature tested, approximately 990°C.

The temperature corresponding to a 5wt% loss provides insight into the onset of significant thermal degradation, and a key indicator of material stability under different environment conditions. The 5wt% loss temperatures (T_d) of the PGS samples are summarized in Table 8. Under an air atmosphere, the Z1-1 sample (first layer) exhibited the lowest thermal stability, with a T_d of approximately 833°C. In comparison, Z1-2 sample (second layer) and its control (Z1-1-C) exhibited higher T_d values of approximately 847°C and 894°C, respectively. These results indicate that graphene structures in the space-exposed layer (Z1-1) were damaged by AO and UV, resulting in reduced thermal stability. Notably, although less affected than the first layer, the second layer (Z1-2) which was not directly exposed to AO and UV, also exhibited a T_d (~ 847°C) lower than control (T_d ~ 894°C). This suggests that space ionizing radiation such as high energy electrons and protons, penetrated the material stack and degraded underlying

material layers. The third layer, Z1-3, also exhibited a lower T_d compared to its control, further confirming radiation-induced damage in layers not directly exposed to AO or UV. Moisture contents for all the PGS samples were low, remaining below approximately 0.2% (Figure S.21-S.28 in Appendix).

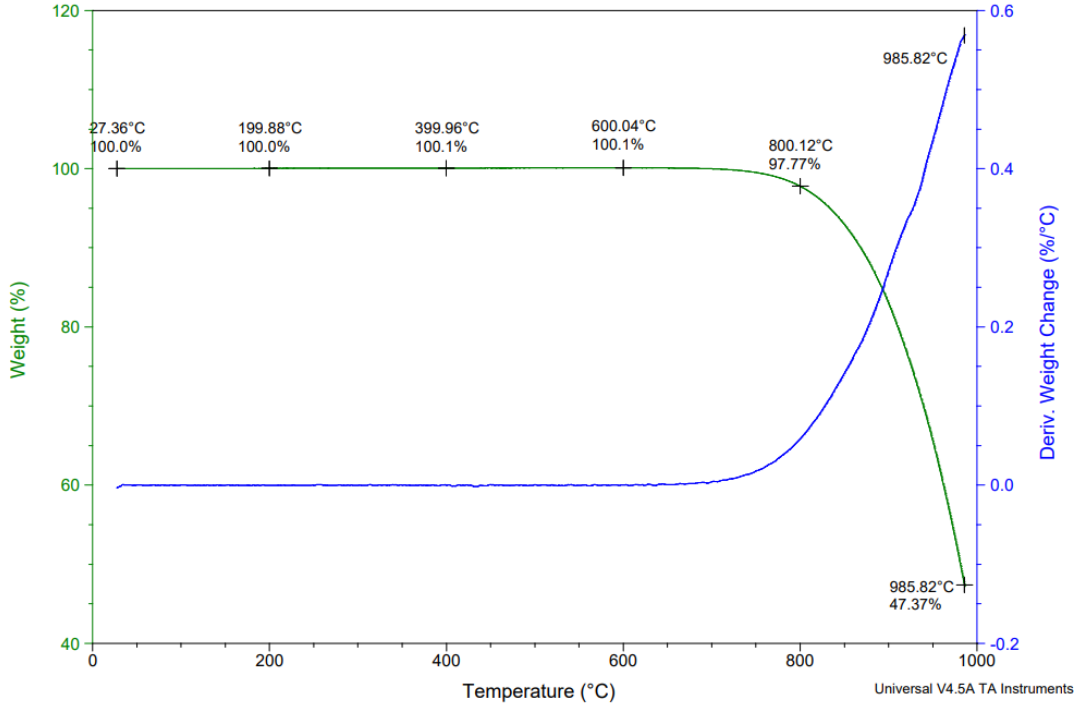

Figure 8. TGA plot of Z1-1 tested in an air atmosphere.

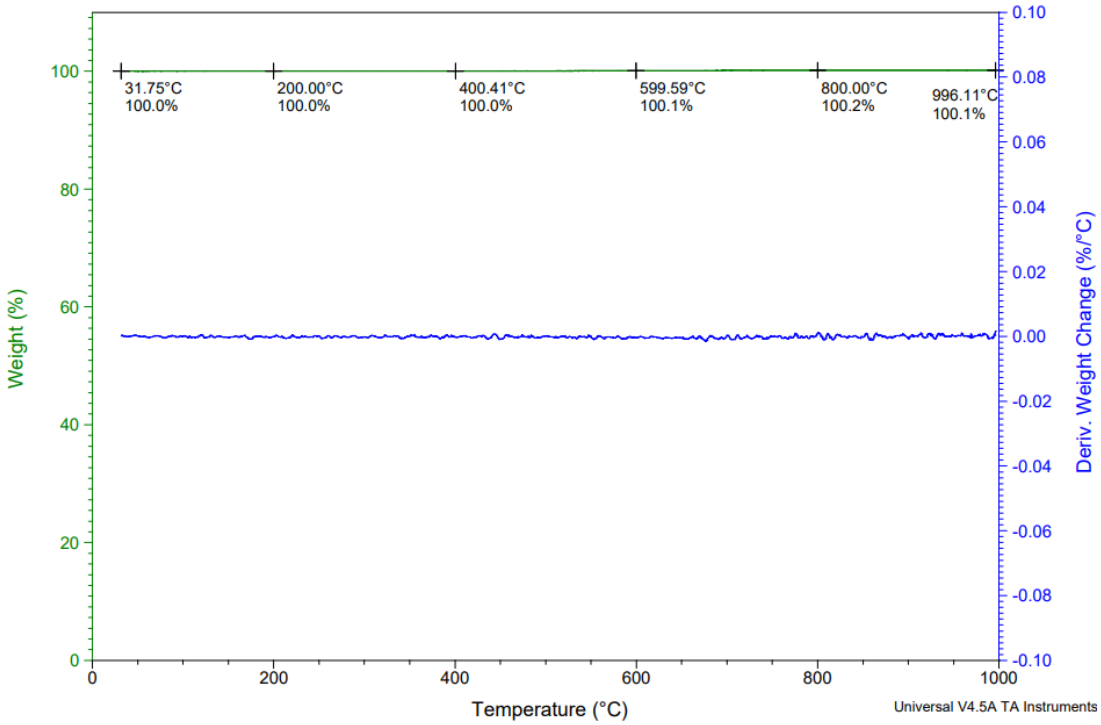

Figure 9. TGA plot of Z1-1 tested in a nitrogen atmosphere.

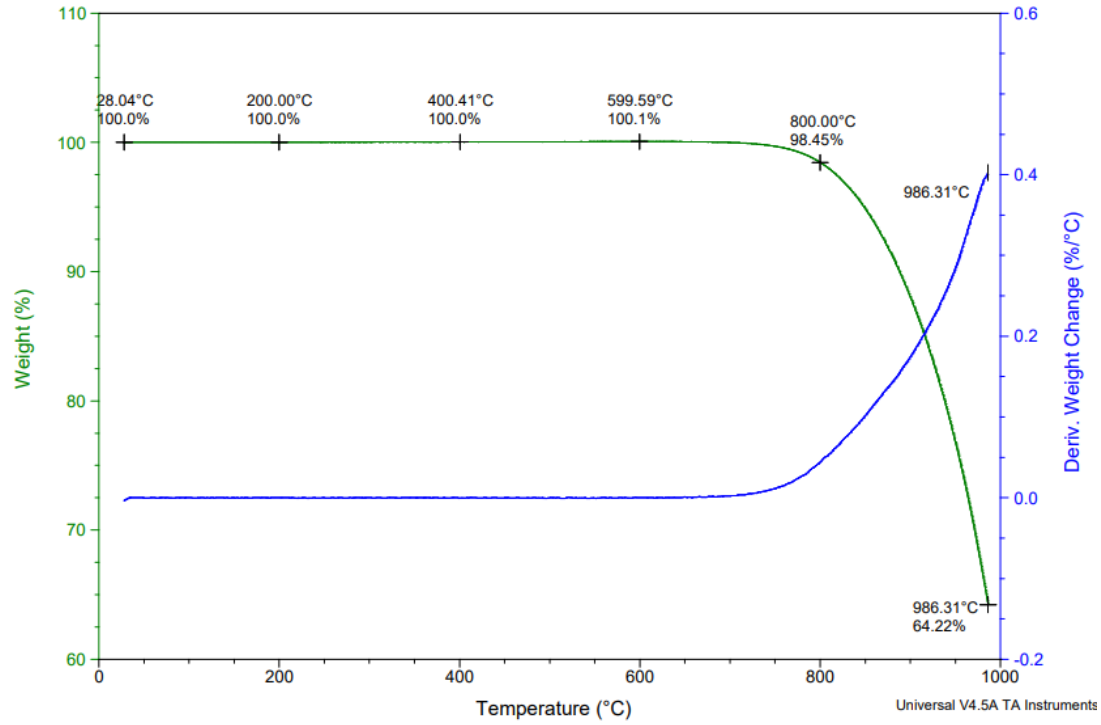

Figure 10. TGA plot of Z1-2 tested in an air atmosphere.

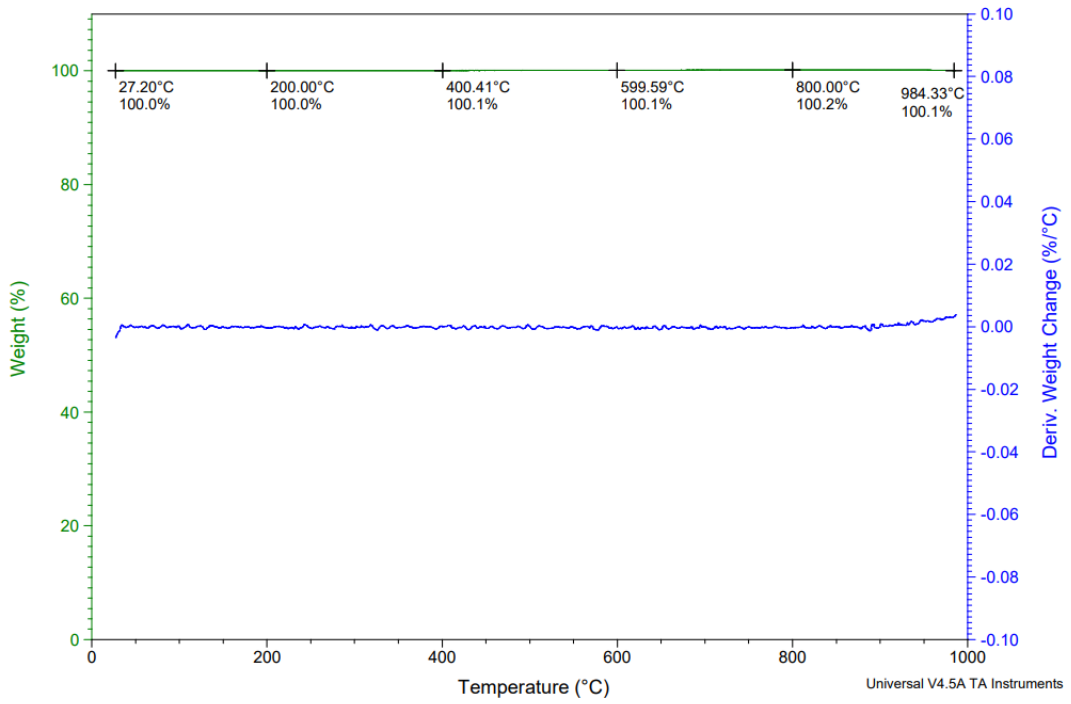

Figure 11. TGA plot of Z1-2 tested in a nitrogen atmosphere.

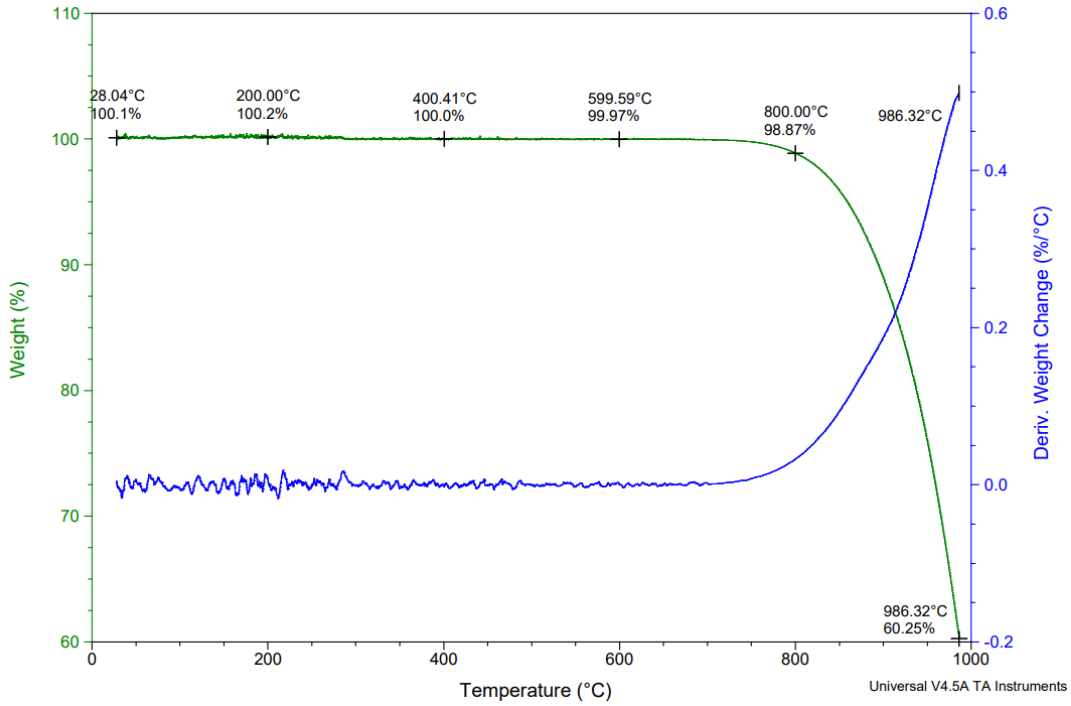

Figure 12. TGA plot of Z1-3 tested in an air atmosphere.

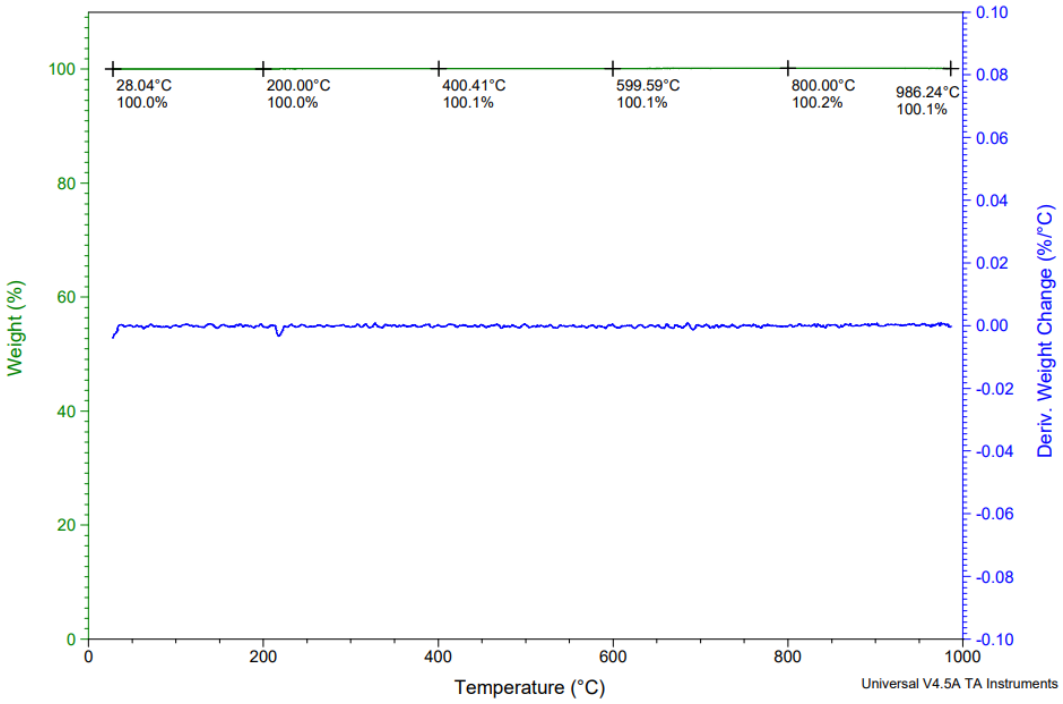

Figure 13. TGA plot of Z1-3 tested in a nitrogen atmosphere.

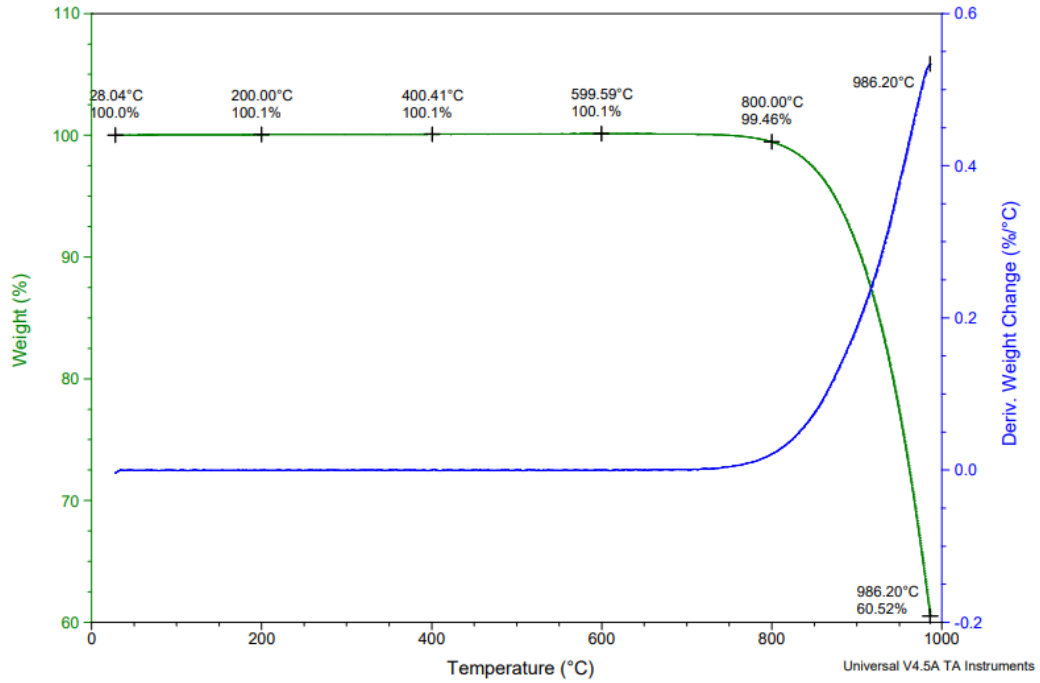

Figure 14. TGA plot of Z1-4 tested in an air atmosphere.

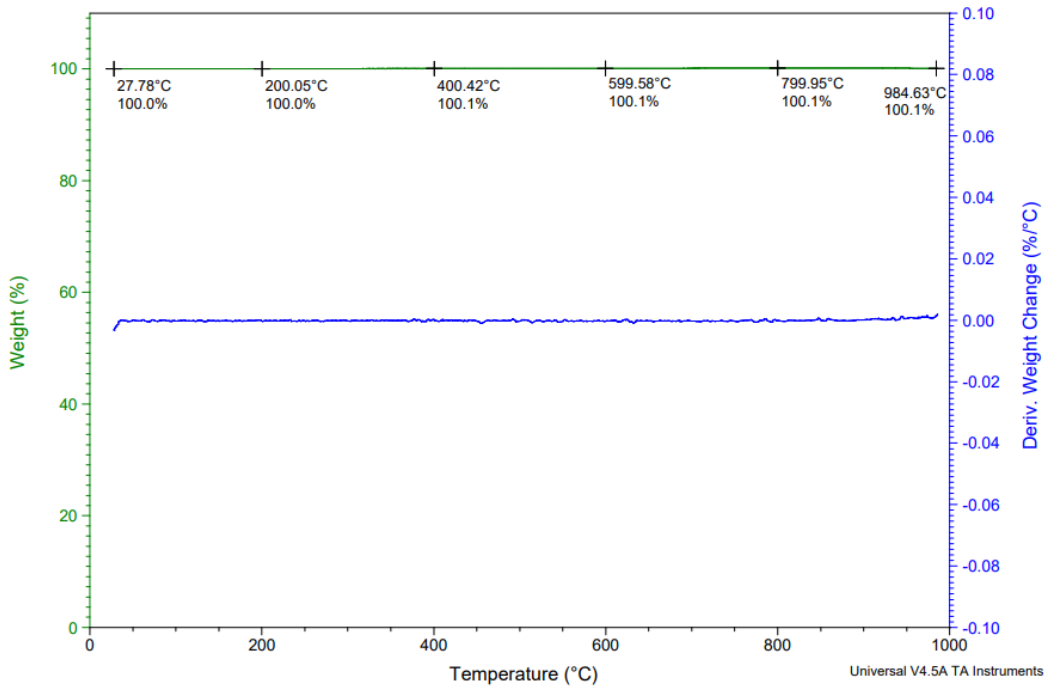

Figure 15. TGA plot of Z1-4 tested in a nitrogen atmosphere.

Table 8: 5 wt.% loss temperature (T_d) for PGS in air atmospheres.

Sample	Atmosphere	5 wt.% loss temperature (°C)
Z1-1	Air	833.1
Z1-2	Air	847.1
Z1-1-C	Air	894.3
Z1-3	Air	858.4
Z1-3-C	Air	896.2
Z1-4	Air	873.1
Z1-4-C	Air	-

Note: Data for some control samples are unavailable.

Figures 16–19 and Figures S.29–S.37 (in Appendix) illustrate the thermal decomposition behavior of the composite samples by showing the weight change at 200°C intervals under the tested atmospheric conditions. Under air, multiple thermo-oxidative decomposition peaks were observed. Significant weight loss began near 400°C, whereas only minimal weight loss occurred at lower temperatures (around 200°C), indicating relatively high thermal stability in this range.

As temperature increased, decomposition accelerated, exhibiting a pronounced decomposition peak near 550°C and a most dominant decomposition peak near 800°C. These multiple peaks correspond to thermo-oxidative degradation of epoxy molecules and graphene structures. Nearly complete decomposition occurred by the end of the heating cycling, leaving less than 1wt% residual char.

Under a nitrogen atmosphere, the composite samples exhibited minimal weight loss up to approximately 400°C, above which a rapid decomposition step initiated. The total weight loss reached approximately 20wt%, corresponding to the thermal degradation of aliphatic segments within polymer matrix. Between 600°C and 800°C, additional weight loss was minimal, indicating a transition to a more statable decomposition regime. By the end of test at 990°C, the remaining mass was approximately 20 to 30 wt.%, representing the formation of aromatic char.

The T_d of the composites are summarized in Table 9. Overall, the composite samples exhibited lower 5 wt.% loss temperatures, ranging from approximately 390°C to 406°C, compared to the PGS samples. In addition, T_d values measured in air were slightly higher than those measured in nitrogen. A trend similar to that observed in the PGS stacks was also evident in the composite stacks. Under air, the Z2-1 sample (first layer) displays a lower T_d than both Z2-2 (second layer) and Z2-2C (control), indicating reduced thermal stability due to AO and UV-induced damage. Furthermore, the Z2-2 (second layer) exhibited a lower T_d than Z2-2C (control), providing additional evidence of radiation-induced degradation in unexposed layers. Moisture contents for all the composite samples were approximately 0.4–0.5 wt.% (Figure S.38-S.48 in Appendix).

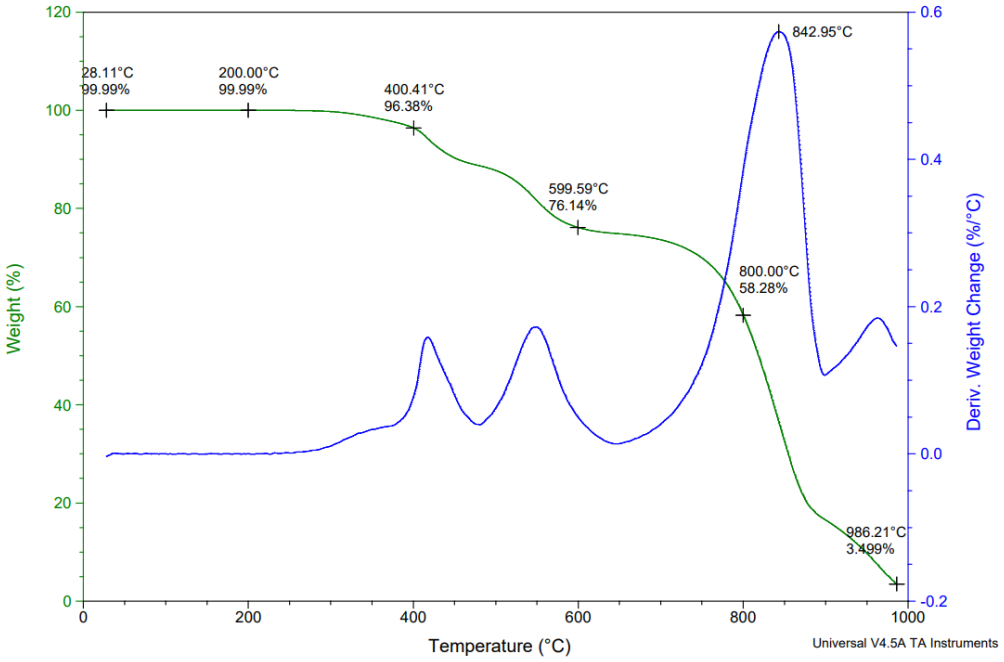

Figure 16. TGA plot of Z2-1 tested in an air atmosphere.

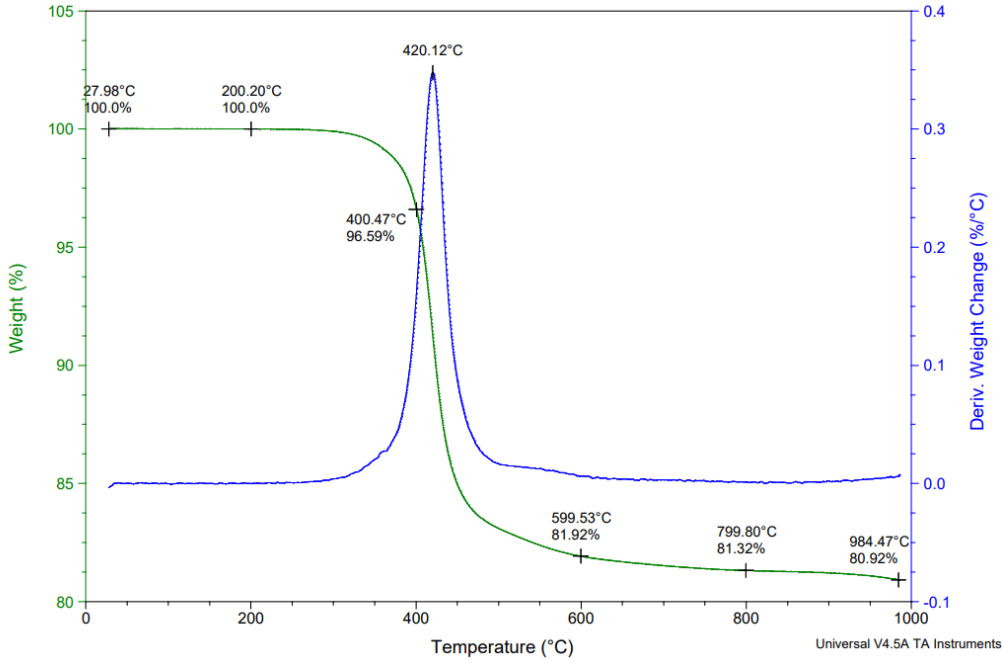

Figure 17. TGA plot of Z2-1 tested in a nitrogen atmosphere.

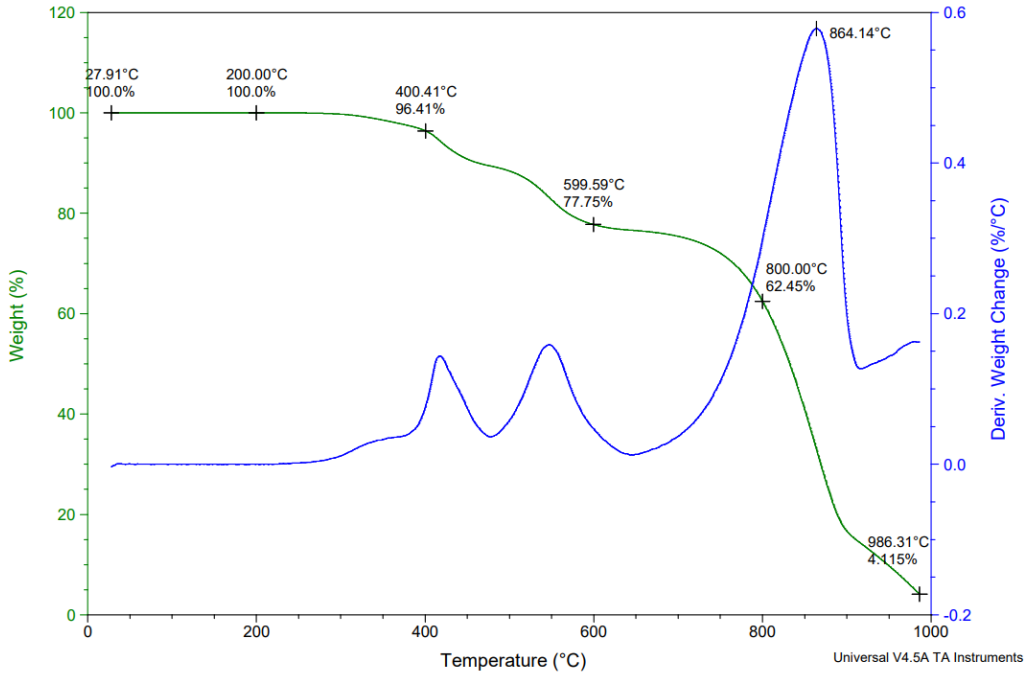

Figure 18. TGA plot of Z2-2 tested in an air atmosphere.

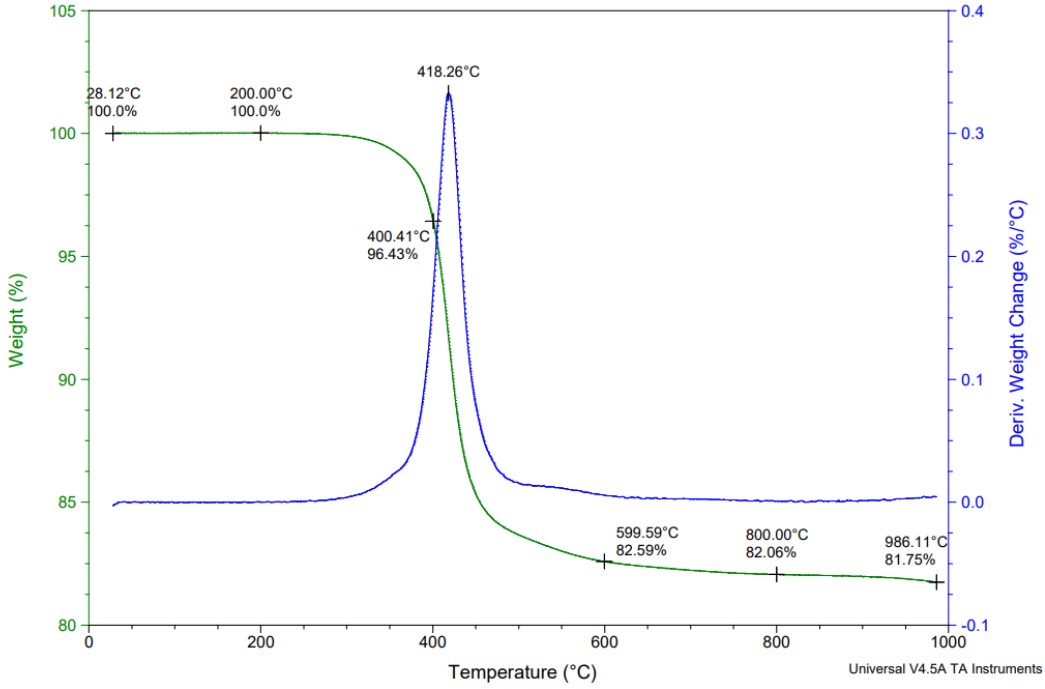

Figure 19. TGA plot of Z2-2 tested in a nitrogen atmosphere.

Table 9: 5 wt.% loss temperature (T_d) for composite samples in air and nitrogen atmospheres.

Sample	Atmosphere	5 wt.% loss temperature (°C)
Z2-1	Air	409.5
	Nitrogen	406.6
Z2-2	Air	411.0
	Nitrogen	406.0
Z2-C	Air	426.6
	Nitrogen	-
Z3-1	Air	399.8
	Nitrogen	396.5
Z3-2	Air	398.5
	Nitrogen	390.6
Z4-1	Air	401.3
	Nitrogen	394.1
Z4-2	Air	394.2
	Nitrogen	391.4
Z4-C	Air	-
	Nitrogen	-

Note: Data for some control samples is unavailable.

3.7 Differential Scanning Calorimetry

The glass transition temperatures (T_g) of the samples were measured by DSC. The composite samples exhibited clear glass transition temperatures, whereas the PGS samples showed no detectable transition. The T_g values obtained from the second scan of the composite samples are summarized in Table 10. The PGS/CF epoxy composite (Z2) had a T_g of approximately 210°C, while the CNT-infused PGS/CF epoxy composites exhibited T_g values of approximately 217–220°C. No significant difference was observed between the T_g values of the space-exposed first layer and the unexposed second layer.

Table 10: Glass transition temperatures (T_g) of composites.

Sample	T_g (°C, 2nd run)
Z2-1	210 ± 0.1
Z2-2	211 ± 0.5
Z2-C	209 ± 0.5
Z3-1	220 ± 0.1
Z3-2	218 ± 2.5
Z3-C	-
Z4-1	218 ± 2.4
Z4-2	217 ± 1.5
Z4-C	-

Note: Data for some control samples is unavailable.

3.8 Thermal conductivity

The thermal conductivities of the PGS and composite samples were measured in both in-plane and out-of-plane directions, and the results are summarized in Figures 20–22 and Table 11. Among the PGS samples, Z1-3 exhibited approximately a 30% reduction in in-plane thermal conductivity, while Z1-4 exhibited no significant change, indicating strong resistance to space radiation-induced degradation (Figure 20). A similar trend was observed in the composite samples: the PGS/CF composites (Z2-1 and Z2-2) exhibited reduced in-plane thermal conductivity, whereas the CNT-infused PGS/CF epoxy composite (Z4-1 and Z4-2) exhibited no significant change within experimental uncertainty (Figure 21). The out-of-plane thermal conductivity results followed the same trend. For the PGS/CF epoxy composite, the thermal conductivity decreased in the order of control sample (Z2-C), second layer (Z2-2) and first layer (Z2-1). In contrast, the CNT-infused PGS/CF epoxy composites (Z4-1, Z4-2 and Z4-C) exhibited no significant differences before and after space exposure (Figure 22). Collectively, these results demonstrate that the CNT-infused PGS/CF epoxy composites exhibit excellent durability in thermal conductivity under space environment.

.

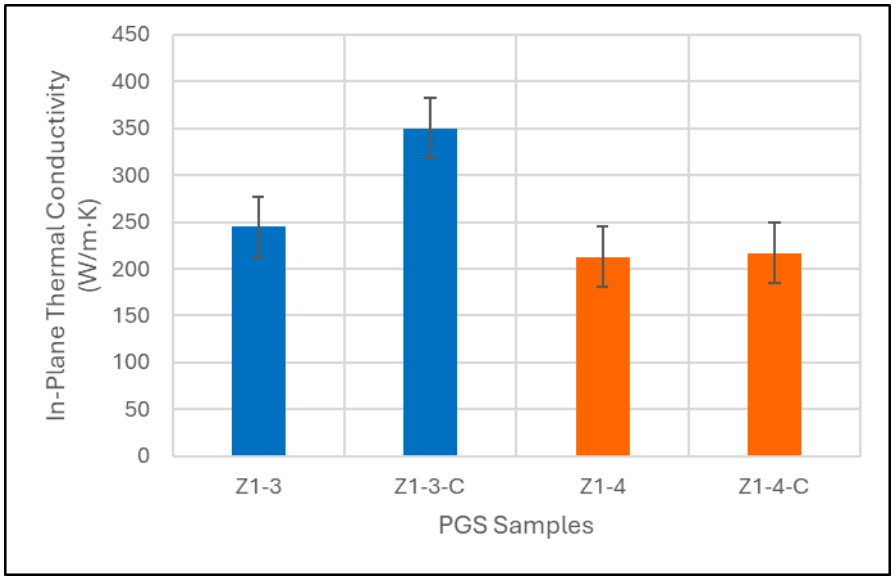

Figure 20. In-plane thermal conductivity of PGS samples.

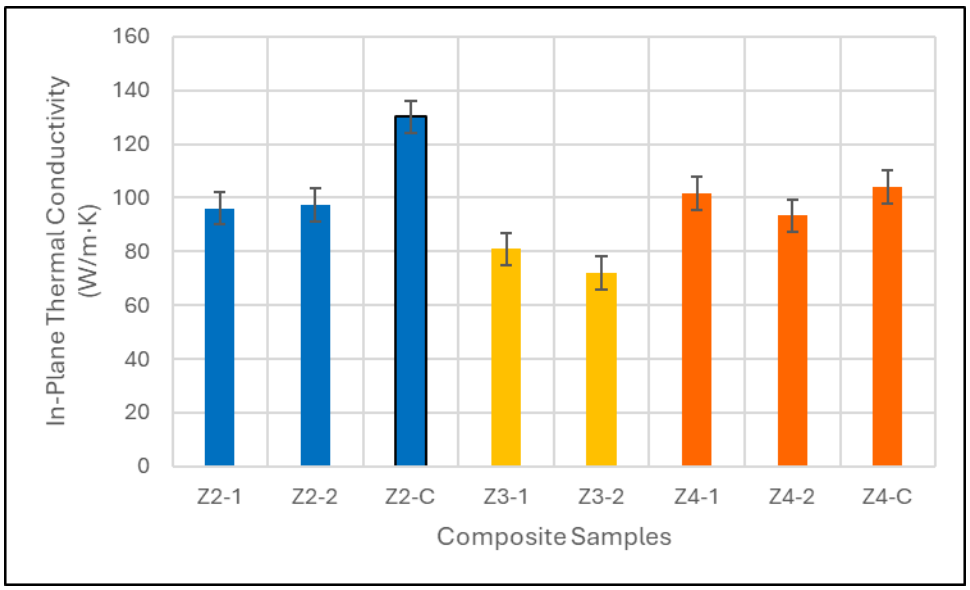

Figure 21. In-plane thermal conductivity of composite samples.

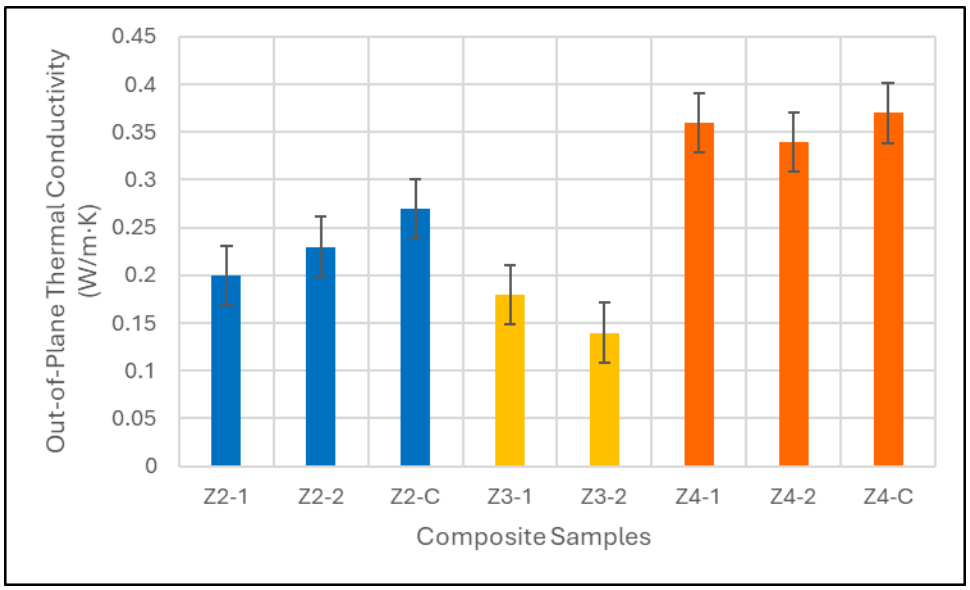

Figure 22. Out-of-plane thermal conductivity of composites.

Table 11: Thermal Conductivity Results for in-plane and out-of-plane.

Samples	In-Plane Thermal Conductivity (W/m·K)	Out-of-Plane Thermal Conductivity (W/m·K)
M17-GK-Z1-1	-	-
M17-GK-Z1-2	-	-
M17-GK-Z1-C	-	-
M17-GK-Z1-3	244.8 ± 15.22	-
M17-GK-Z1-3-C	350.02 ± 11.13	-
M17-GK-Z1-4	212.5 ± 3.83	-
M17-GK-Z1-4-C	216.6 ± 1.22	-
M17-GK-Z2-1	96.03 ± 1.04	0.20 ± 0.00
M17-GK-Z2-2	97.42 ± 0.91	0.23 ± 0.01
M17-GK-Z2-C	130.1 ± 2.76	0.27 ± 0.01
M17-GK-Z3-1	80.97 ± 1.03	0.18 ± 0.00
M17-GK-Z3-2	72.01 ± 3.17	0.14 ± 0.00
M17-GK-Z4-1	101.6 ± 0.69	0.36 ± 0.02
M17-GK-Z4-2	93.34 ± 1.46	0.34 ± 0.01

M17-GK-Z4-C	104 ± 1.32	0.37 ± 0.02

Note: There is no in-plane data for samples Z1-1, Z1-2 and Z1-C and no out-of-plane data for the PGS samples, as they were too thin to be measured within the available sensors' operational range

4. Conclusion

This study evaluated the effect of space environment on novel highly thermally conductive composites including pyrolytic graphite sheet (PGS), PGS/carbon fiber (CF) epoxy composites, and CNT-infused PGS/CF epoxy composites through post-flight characterization following 159 days of Materials International Space Station Experiment (MISSE)-17 flight in low Earth orbit (LEO). The graphene-based PGS demonstrated exceptional structural resilience, exhibiting negligible mass loss, minimal thermo-optical property change, and only mild oxidation signatures. Although the epoxy matrix composites exhibited slightly greater weight loss of approximately 0.5wt% due to UV and AO-induced erosion and degradation, they largely maintained their thermo-optical performance. Thermal conductivity analysis further supported these findings: CNT-infused PGS/CF epoxy composites retained high thermal conductivities with limited degradation, indicating that CNT networks help stabilize thermal transport pathways even as the matrix undergoes radiation-induced damage. In summary, these findings highlight that graphene-derived PGS and CNT-infused composites are strong candidates for lightweight radiators and thermal management hardware in space applications. PGS offers superior environmental durability, while CNT architectures enable multifunctional composites that preserve critical thermo-optical and thermal performance under erosive LEO conditions. Continued advancement of improving out-of-plane thermal conductivity is expected to further enhance the performance of next-generation lightweight radiators for deep space exploration missions.

5. References

1. K. de Groh, B. Banks, “MISSE-Flight Facility Polymers and Composites Experiments 1-4 (PCE 1-4),” (NASA/TM-20205008863) National Aeronautics and Space Administration, February 2021.
2. J. H. Kang, K. Gordon, R. Bryant, W. K. Wilkie, K. de Groh, O. Stohlman, J. Fernandez, J. Warren, G. Dean, N. Schneider, T. Denkins, A. Stark, P. Brown, and M. Chamberlain, "Space Environmental Damage Assessment on Sail/Deorbit Materials in Low Earth Orbit," The 6th International Symposium on Space Sailing, New York, NY, US, June 8, 2023.
3. J. H. Kang, K. Gordon, D. Ward, G. Belancik, P. Jagtap, G. Sauti, “Highly Thermally Conductive Hybrid Carbon Fiber Polymer Composite for Radiator Application,” 52nd International Conference on Environmental System (ICES), Calgary, Canada, July 16-20, 2023, 10pp.
4. G. Belancik, G., Schuh, M., Jan, D., and Jagtap, P., “Evaluation Capabilities of the Carbon Dioxide Deposition System,” 50th International Conference on Environmental Systems Proceedings, ICES, online, July 2020.
5. ASTM Standard E490-22, “Standard Solar Constant and Zero Air Mass Solar Spectral Irradiance Tables,” ASTM International, West Conshohocken, PA, 2022.
6. Han, J. H., Kim, C. G., “Low earth orbit space environment simulation and its effects on graphite/epoxy composites,” Composite Structures, 72(2), 218–226. 2006
7. Fujimoto, K., Satoh, K., Shioya, T., Seki, N., Fujita K., “Degradation of materials by high-energy atomic oxygen,” JSME International Journal, Series A: Solid Mechanics and Material Engineering. 46, 283–289, 2003.

6. Appendix

6.1 OM Images

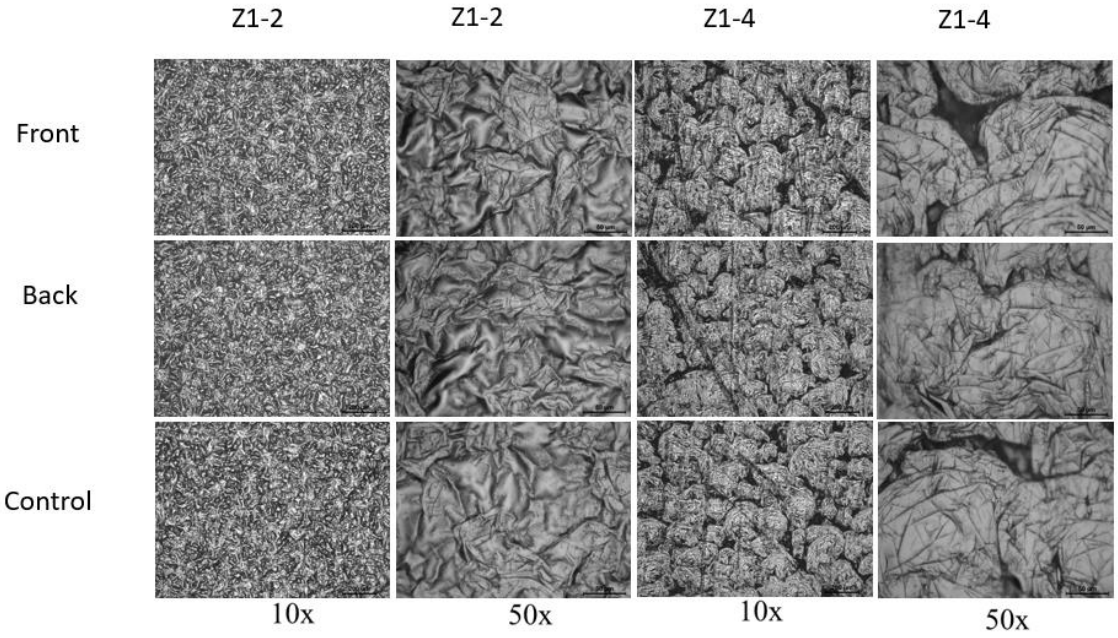

Figure S.1. OM images of Z1-2, Z1-4.

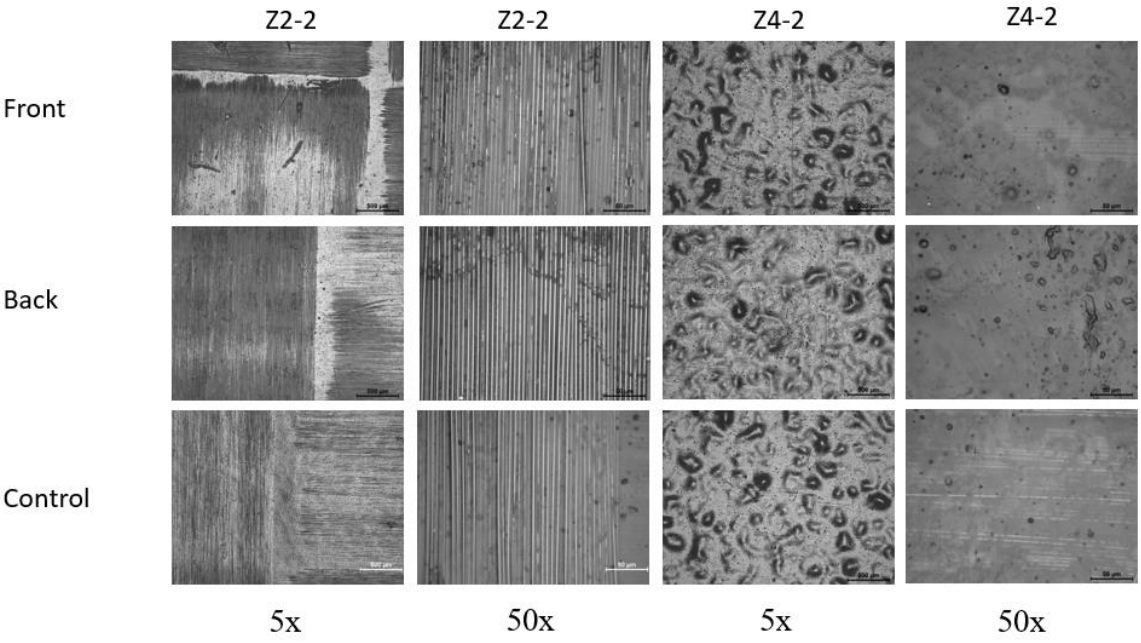

Figure S.2. OM images of Z2-2, Z4-2.

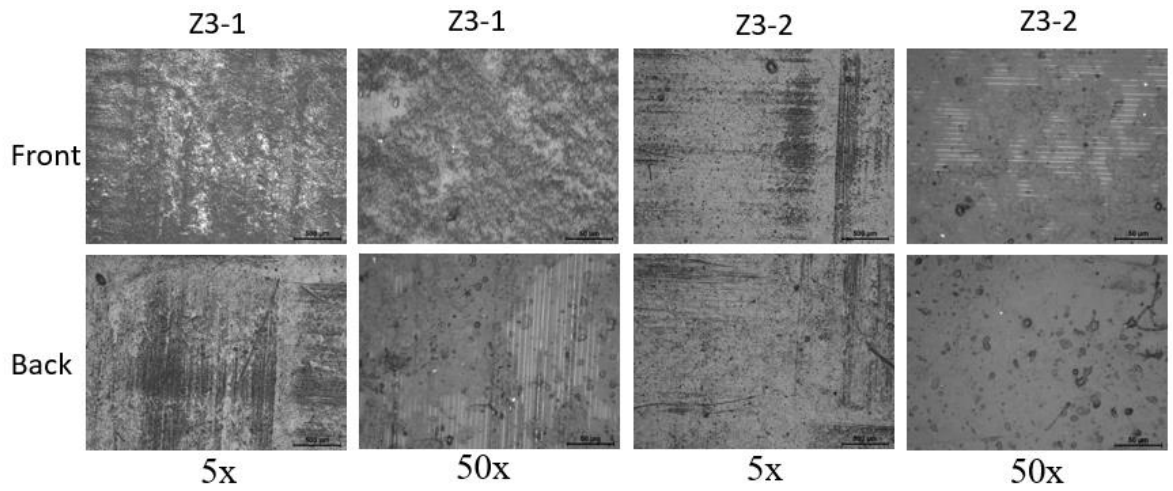

Figure S.3. OM images of Z3-1, Z3-2.

6.2 Topographical Images

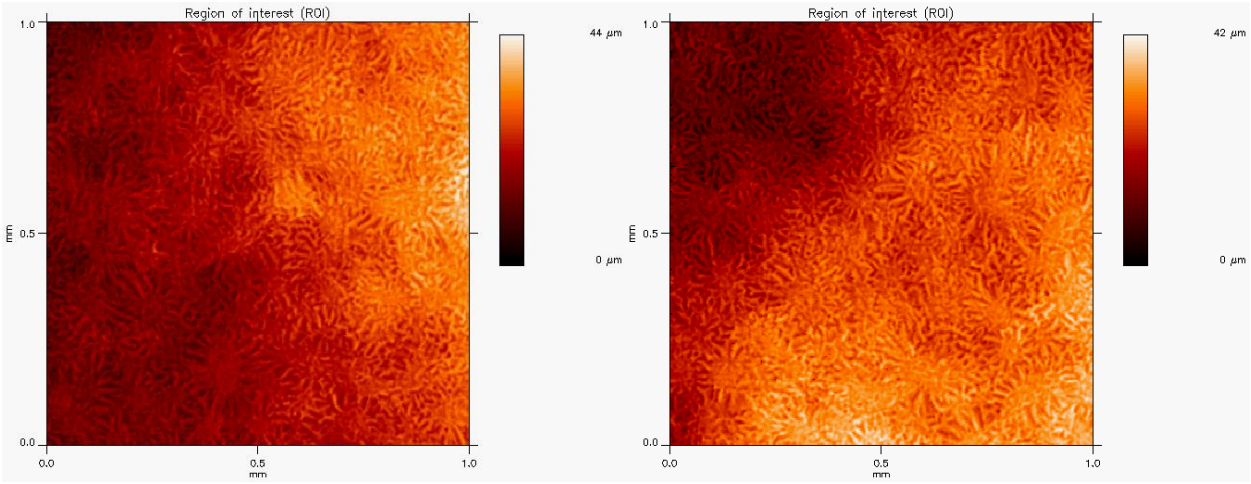

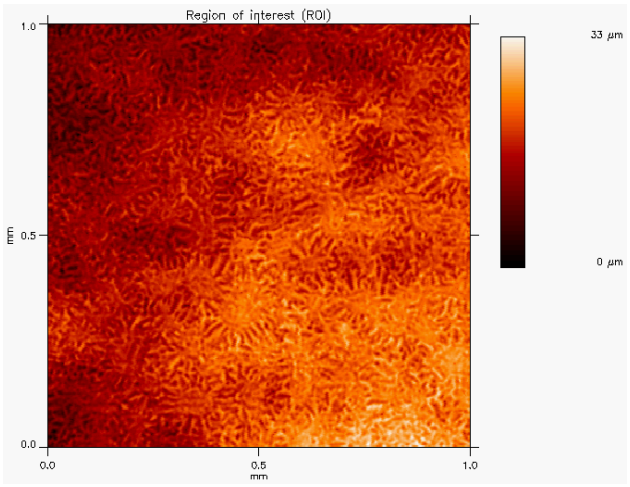

Figure S.4. Surface topography of (a) Z1-1, (b) Z1-2 and (c) Z1-C.

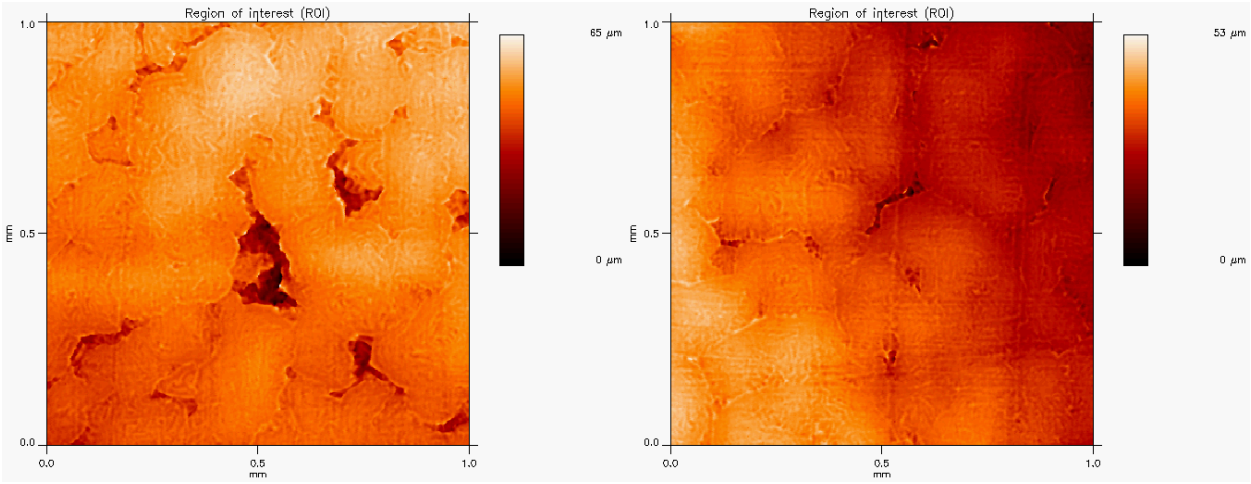

Figure S.5. Surface topography of (a) Z1-3 and (b) Z1-C.

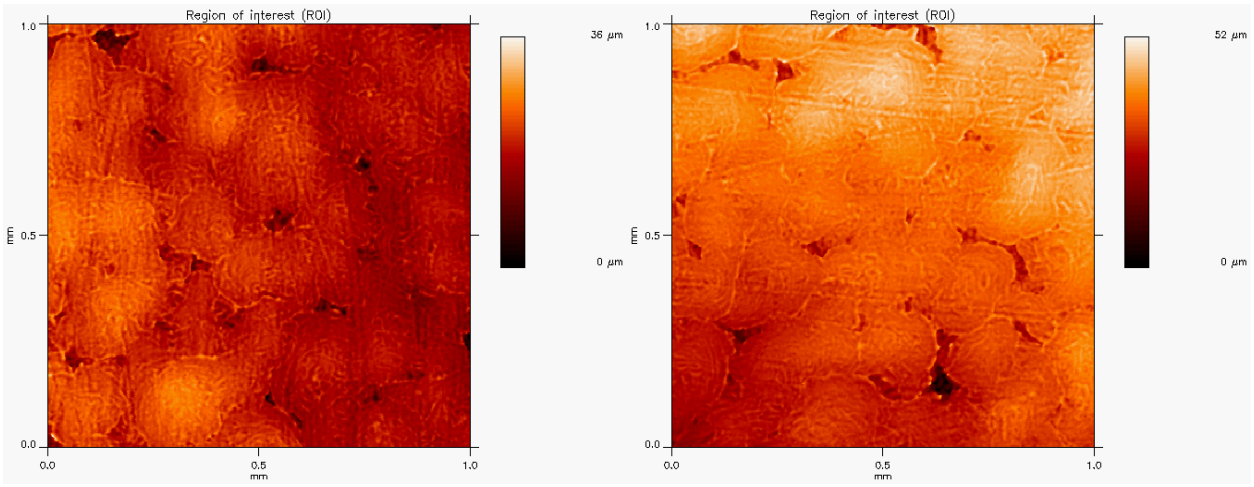

Figure S.6. Surface Topography of (a) Z1-4 and (b) Z1-4-C.

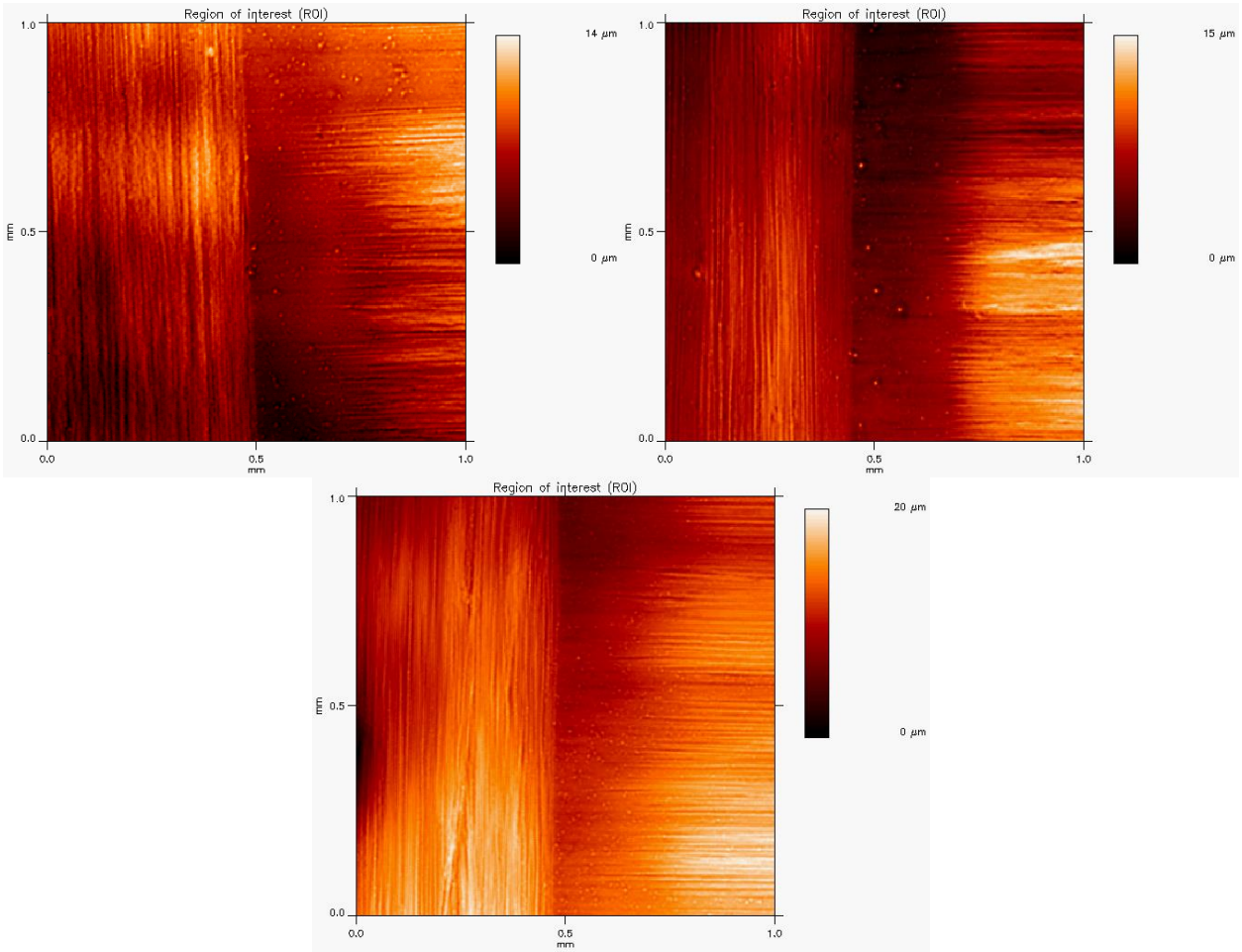

Figure S.7. Surface topography of composite samples: Z2-1, Z2-2, Z2-C.

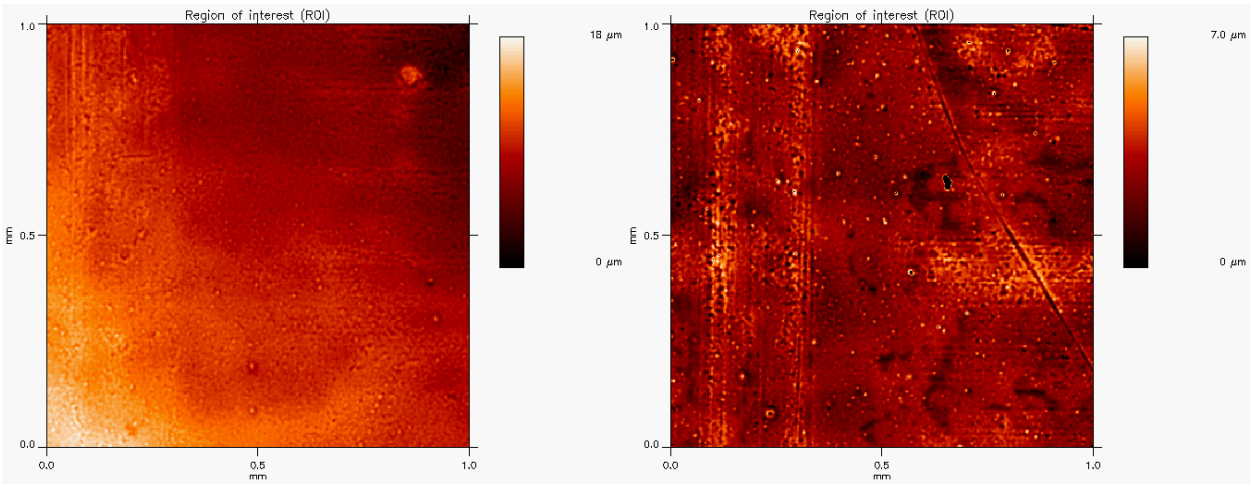

Figure S.8. Surface Topography of Composite samples: Z3-1, Z3-2.

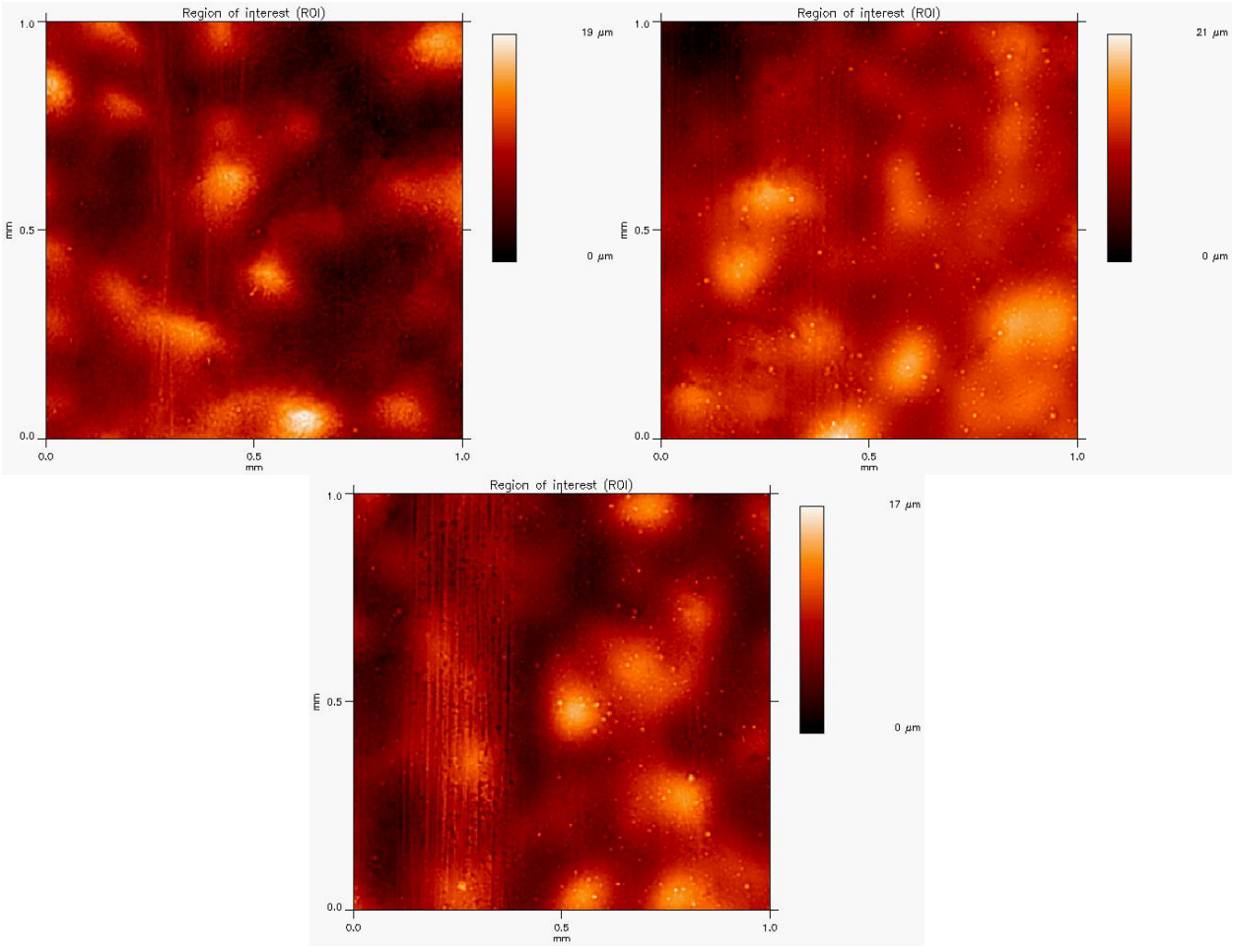

Figure S.9. Surface Topography of Composite samples: Z4-1, Z4-2, Z4-C.

6.3 UV/VIS/NIR Spectroscopy

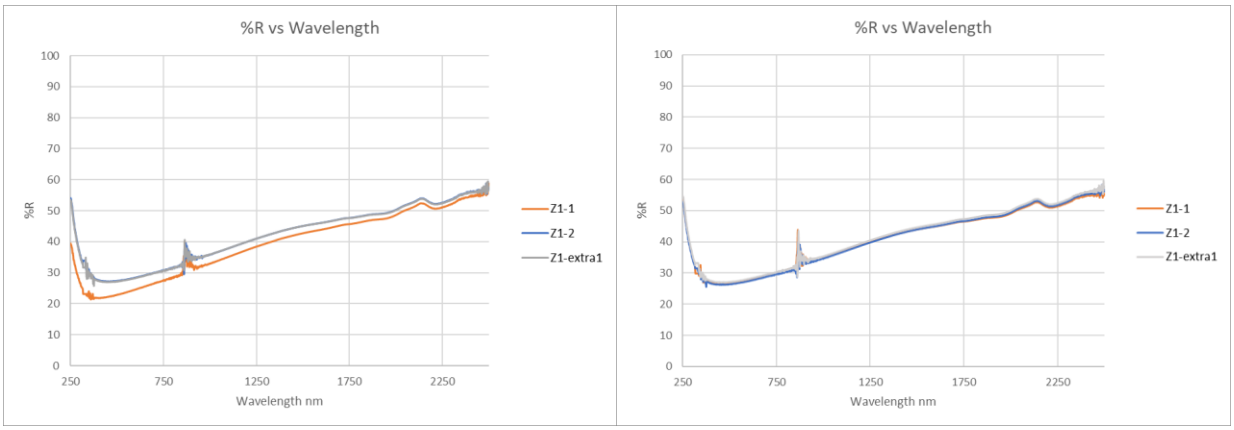

Figure S.10. UV/VIS/NIR spectra of Z1-1, Z1-2 and Z1-1-C. Front (left) and back sides (right).

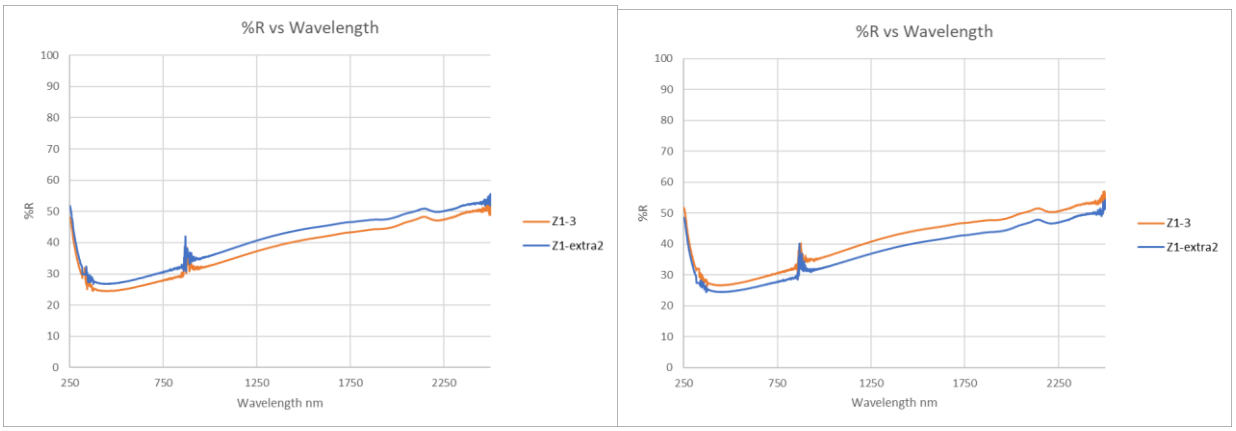

Figure S.11. UV/VIS/NIR spectra of Z1-3 and Z1-3-C. Front (left) and back side s(right).

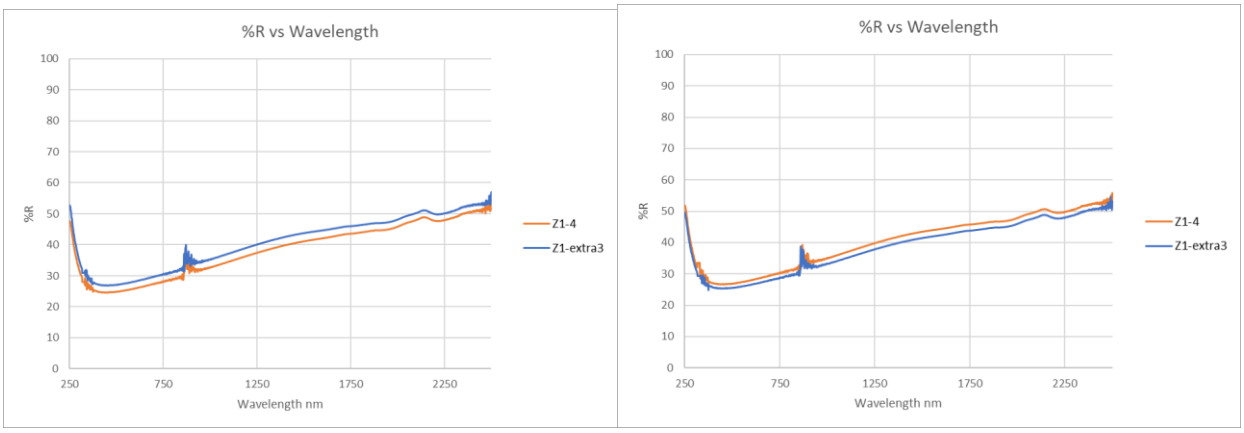

Figure S.12. UV/VIS/NIR spectra of Z1-4 and Z1-4-C. Front (left) and back sides (right).

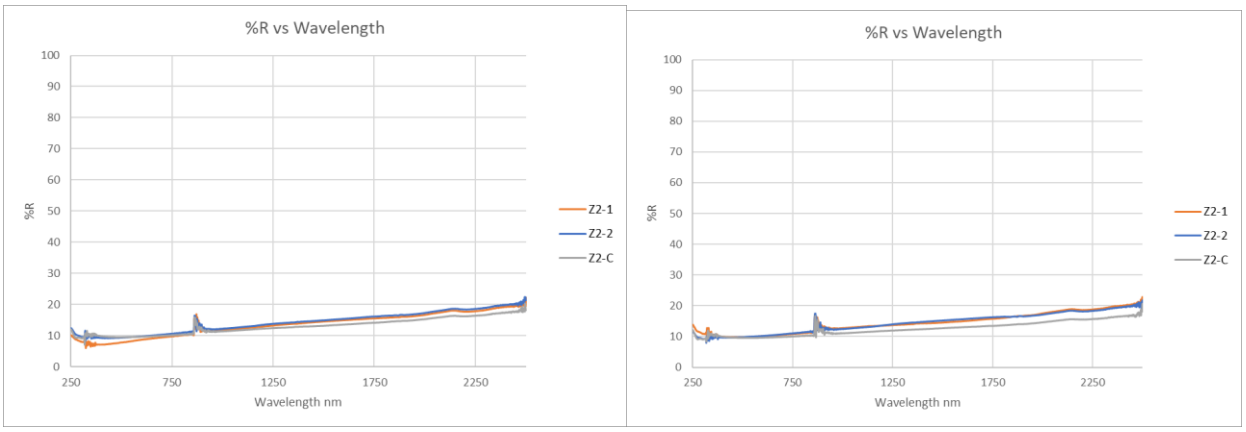

Figure S.13. UV/VIS/NIR spectra of Z2-1, Z2-2 and Z2-C. Front (left) and back sides (right).

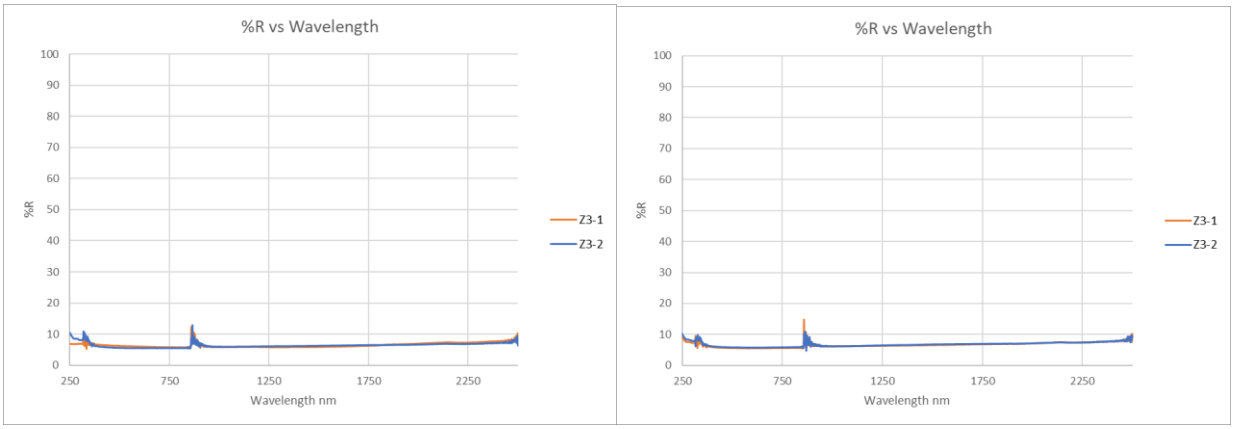

Figure S.14. UV/VIS/NIR spectra of Z3-1 and Z3-2. Front (left) and back sides (right).

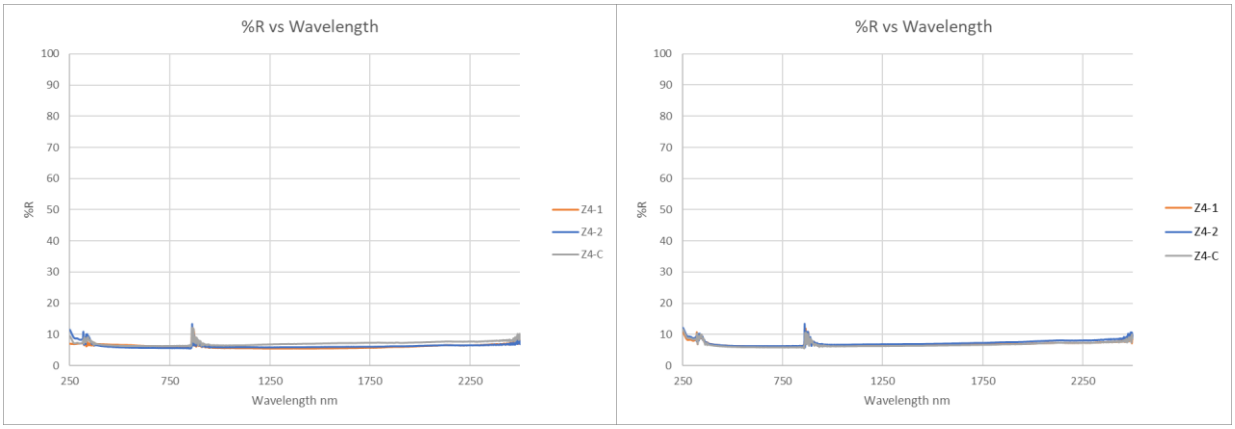

Figure S.15. UV/VIS/NIR spectra of Z4-1, Z4-2 and Z4-C. Front (left) and back sides (right).

6.4 FT-IR

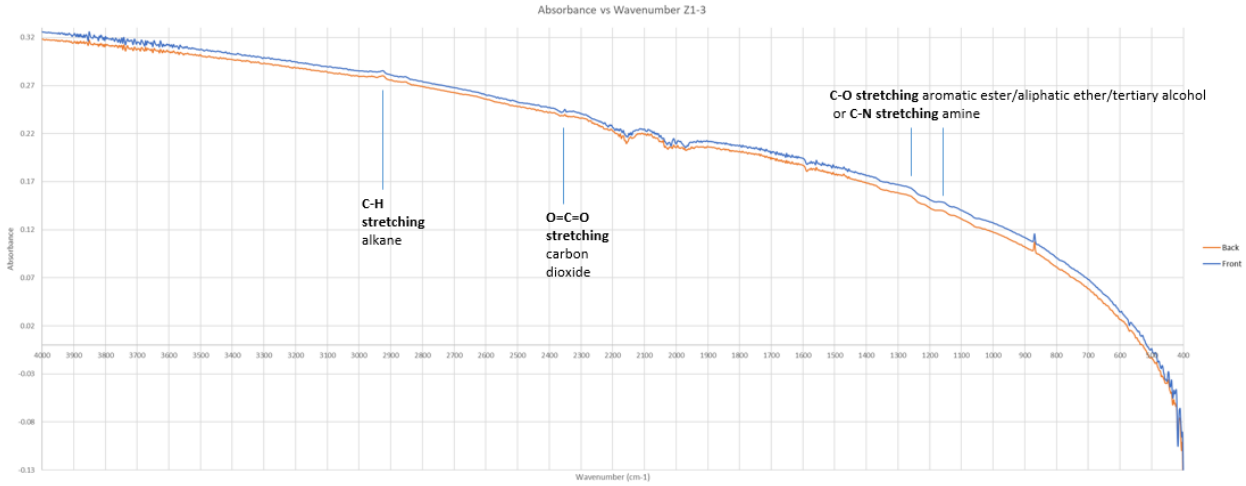

Figure S.16. FT-IR spectra of Z1-3 (front & back).

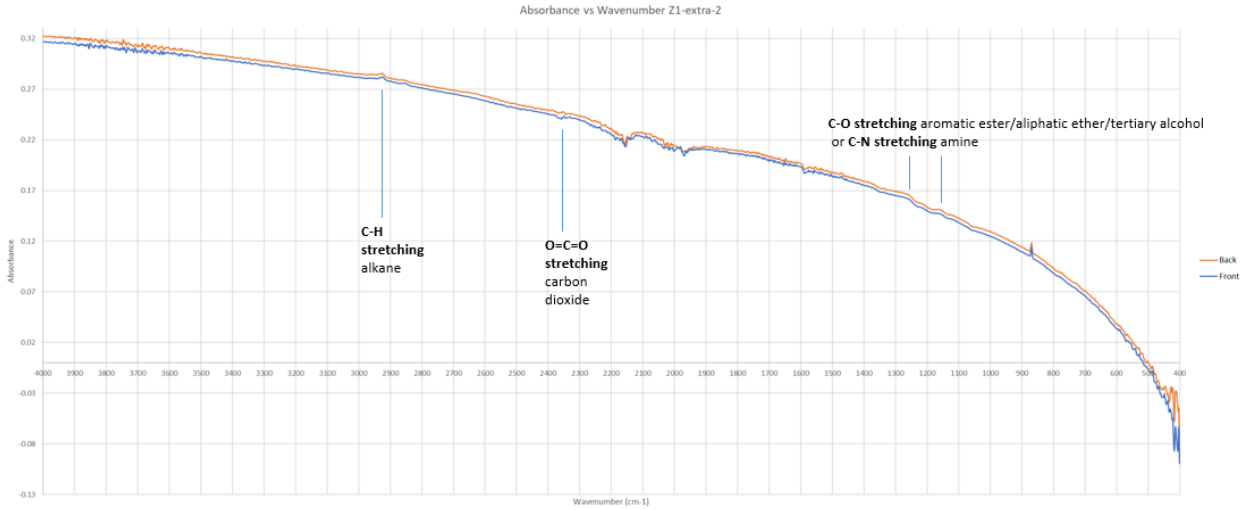

Figure S.17. FT-IR spectra of Z1-3-C (front & back).

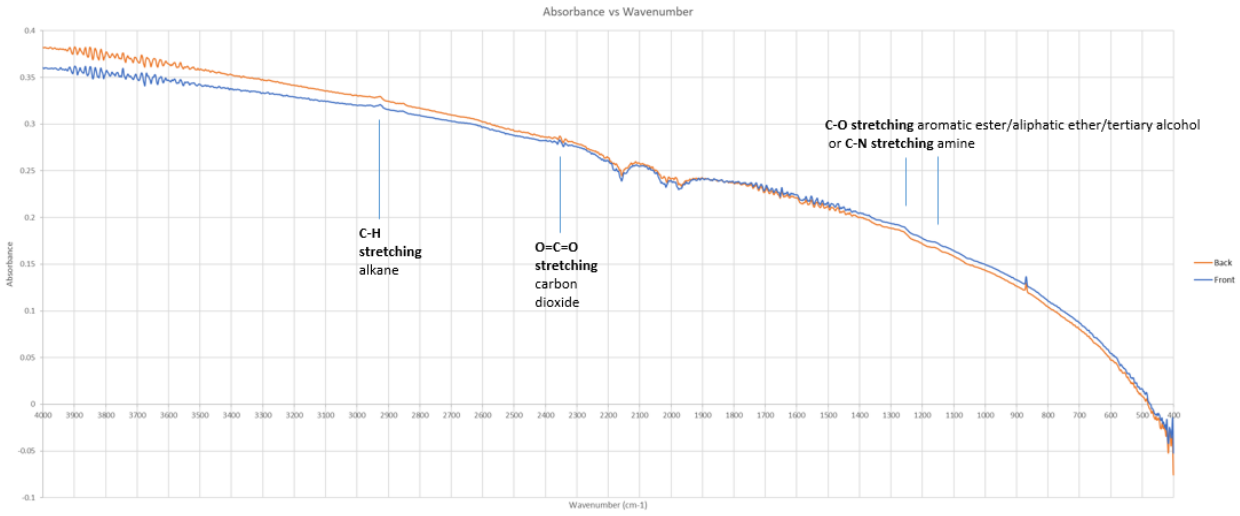

Figure S.18. FT-IR spectra of Z1-4 (front & back).

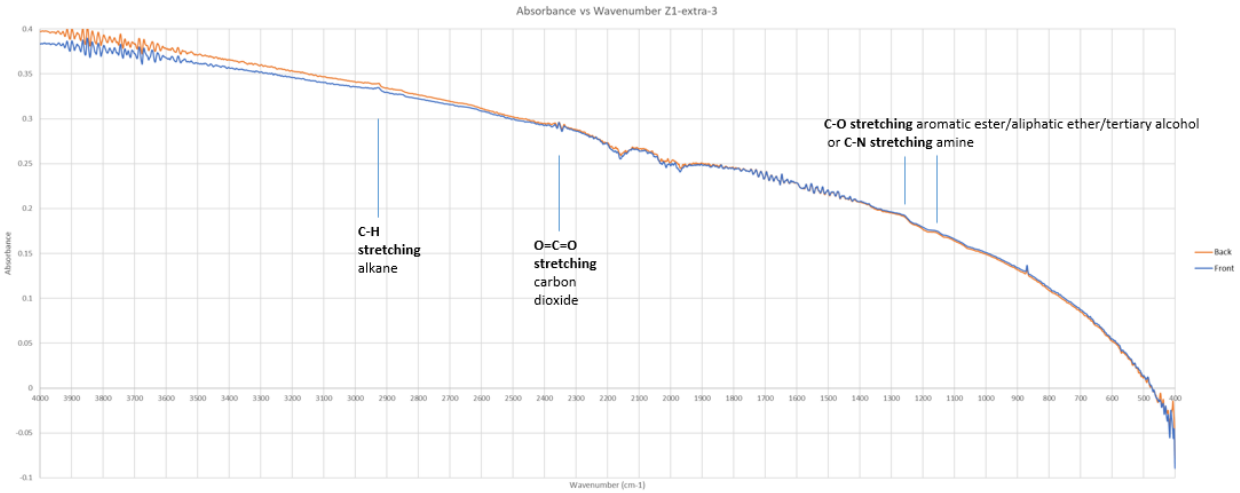

Figure S.19. FT-IR spectra of Z1-4-C (front & back).

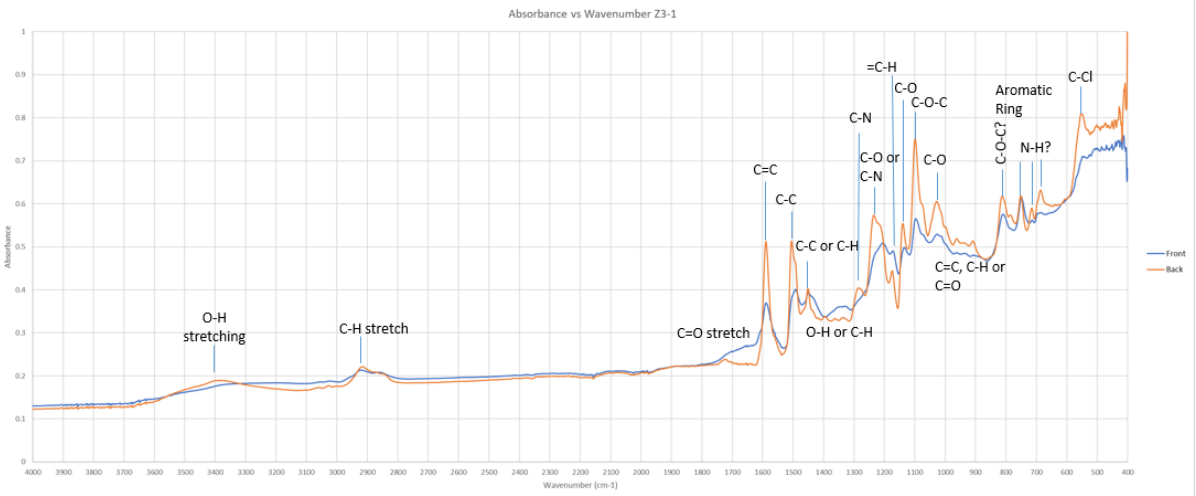

Figure S.20. FT-IR spectra of Z3-1 (front & back).

6.5 TGA

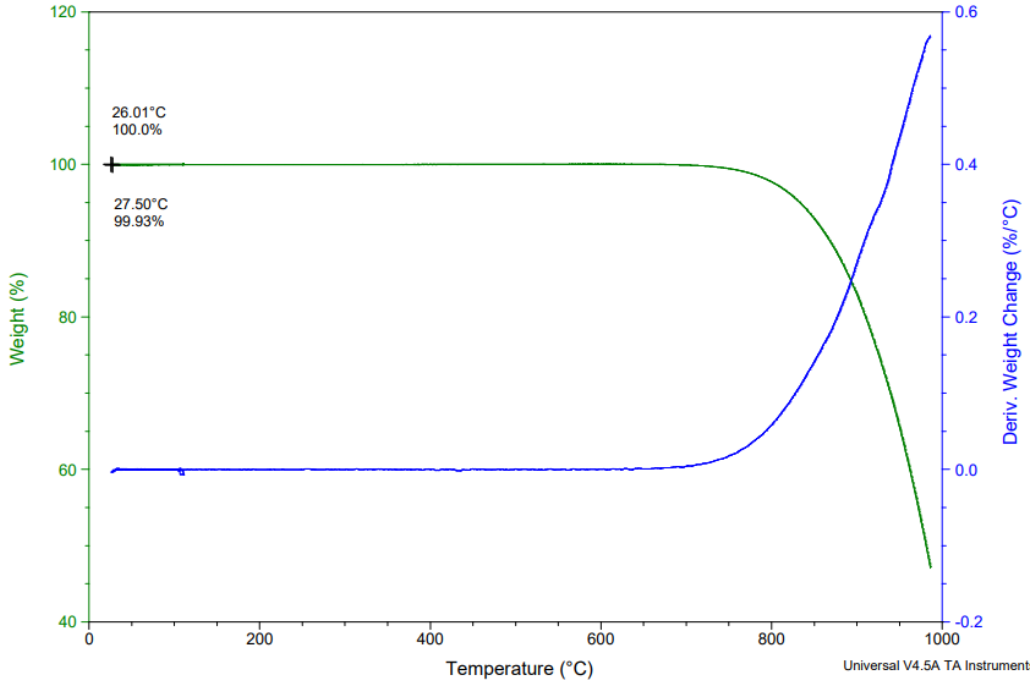

Figure S.21. TGA moisture plot of Z1-1 measured in an air atmosphere.

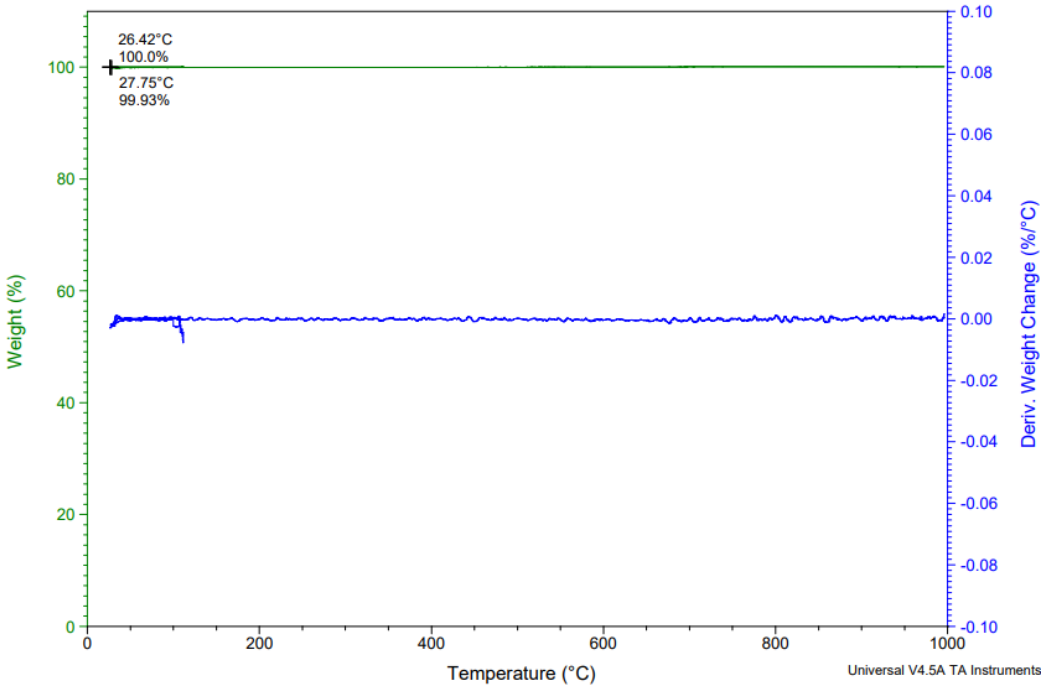

Figure S.22. TGA moisture loss plot of Z1-1 measured in a nitrogen atmosphere.

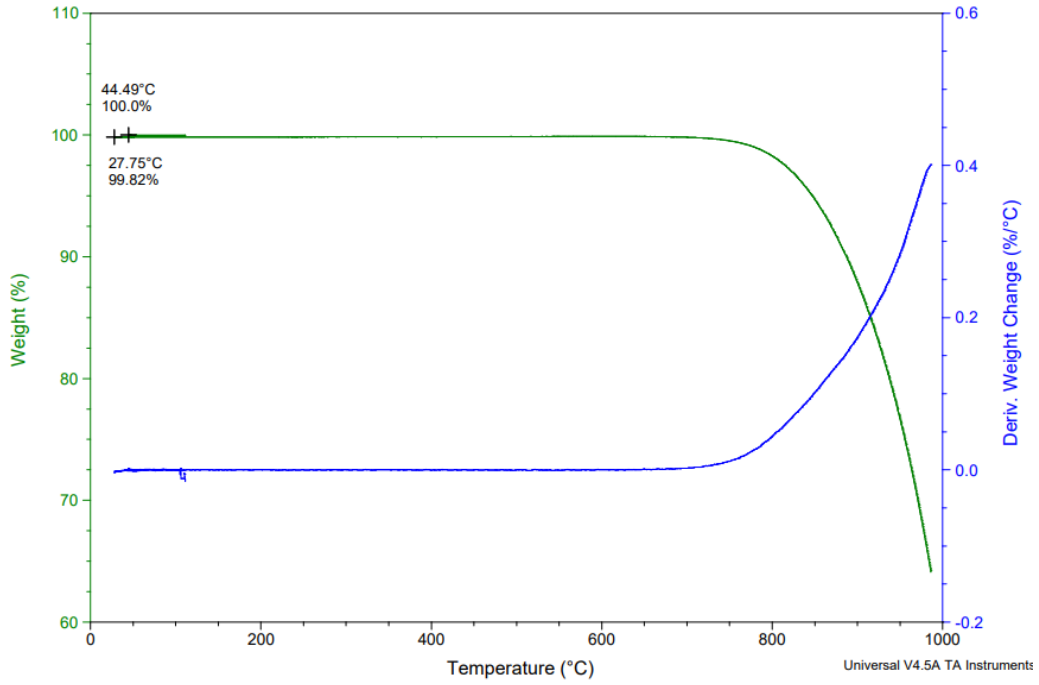

Figure S.23. TGA moisture loss plot of Z1-2 measured in an air atmosphere.

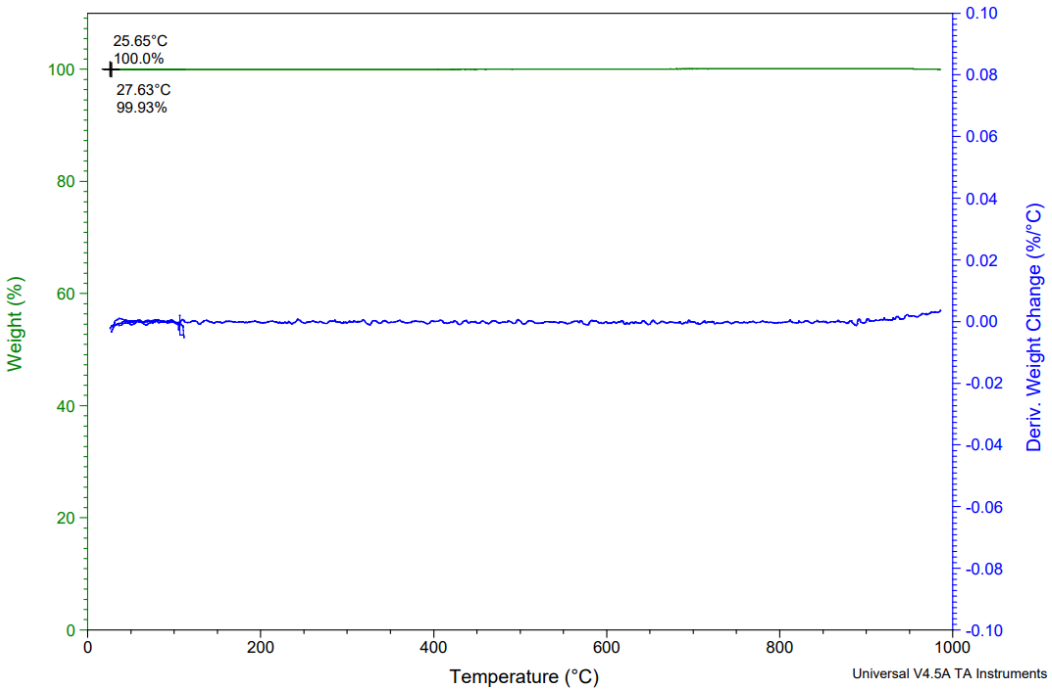

Figure S.24. TGA moisture loss plot of Z1-2 measured in a nitrogen atmosphere.

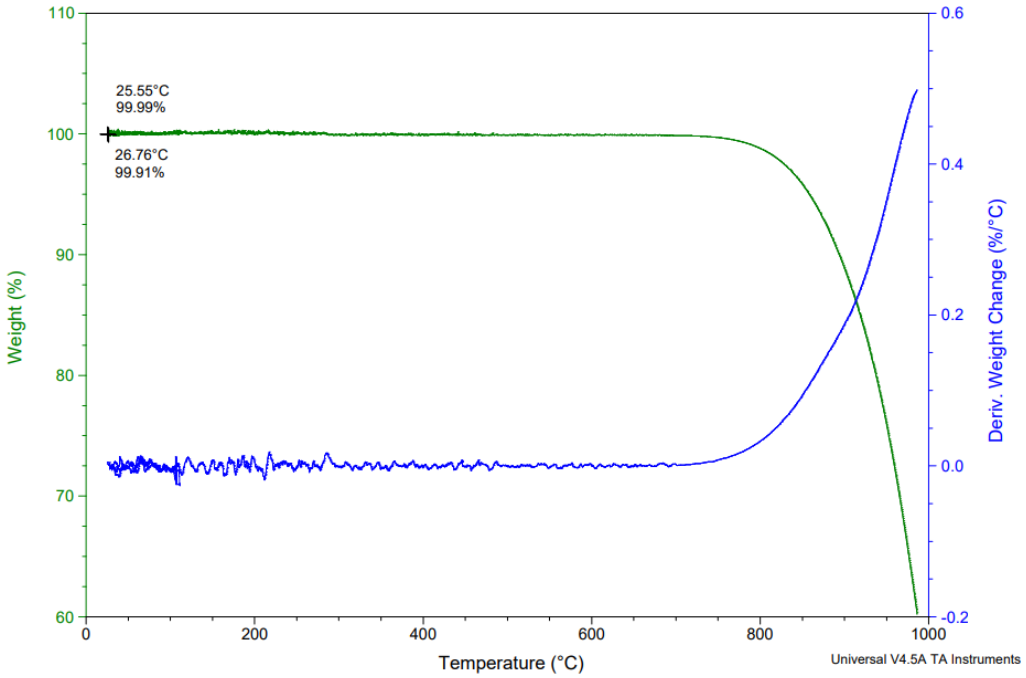

Figure S.25. TGA moisture loss plot of Z1-3 measured in an air atmosphere.

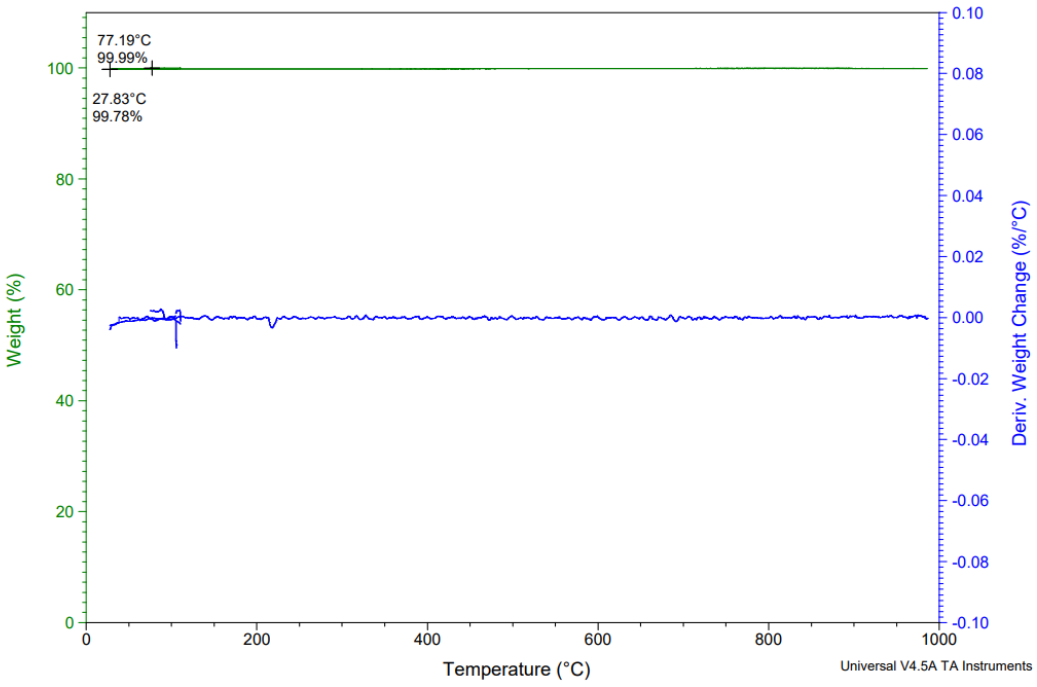

Figure S.26. TGA moisture loss plot of Z1-3 measured in a nitrogen atmosphere.

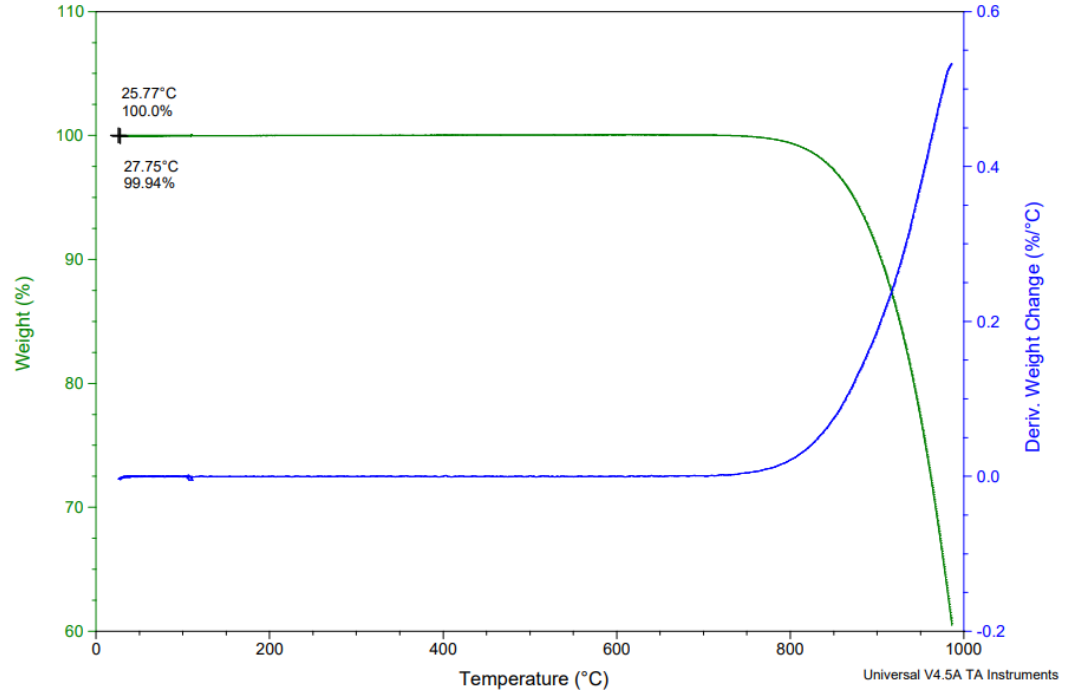

Figure S.27. TGA moisture loss plot of Z1-4 measured in an air atmosphere.

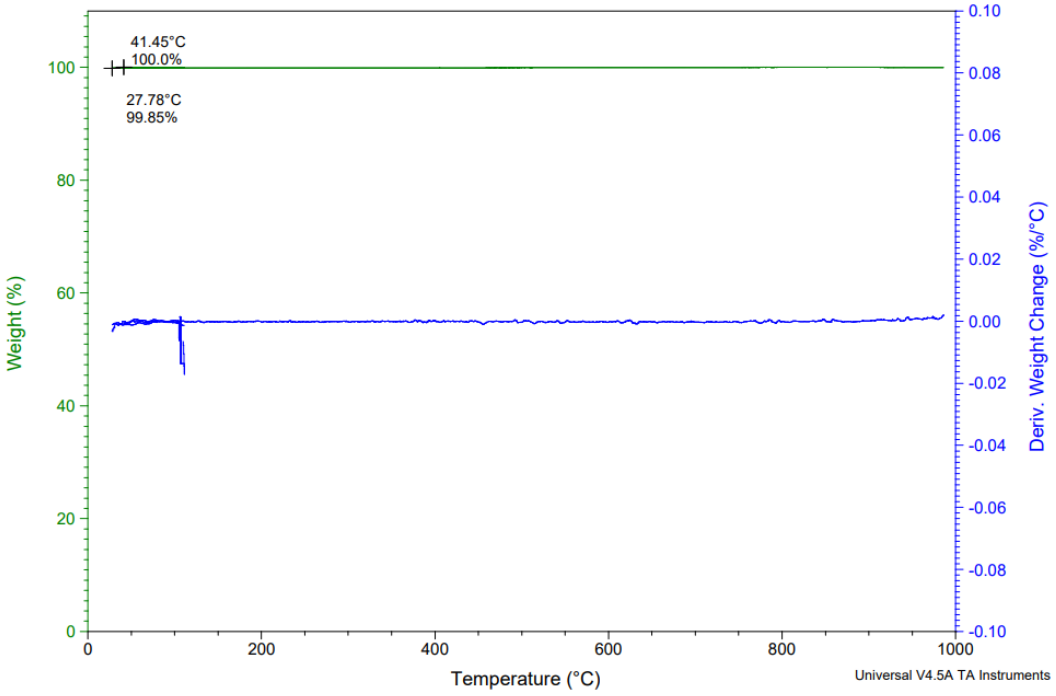

Figure S.28. TGA moisture loss plot of Z1-4 measured in a nitrogen atmosphere.

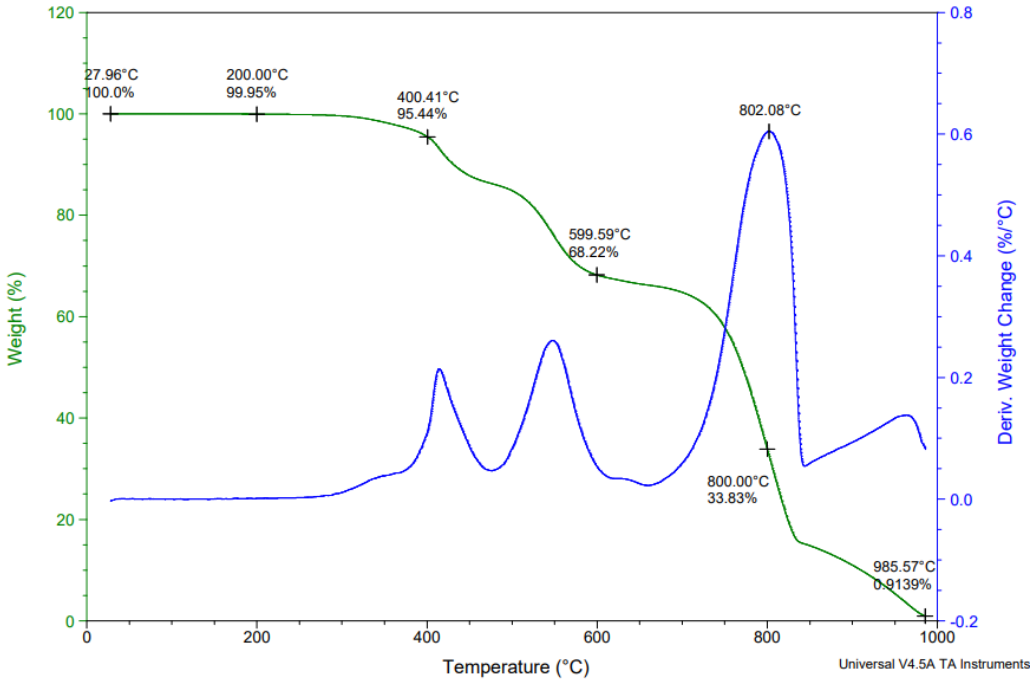

Figure S.29. TGA plot of Z3-1 measured in an air atmosphere.

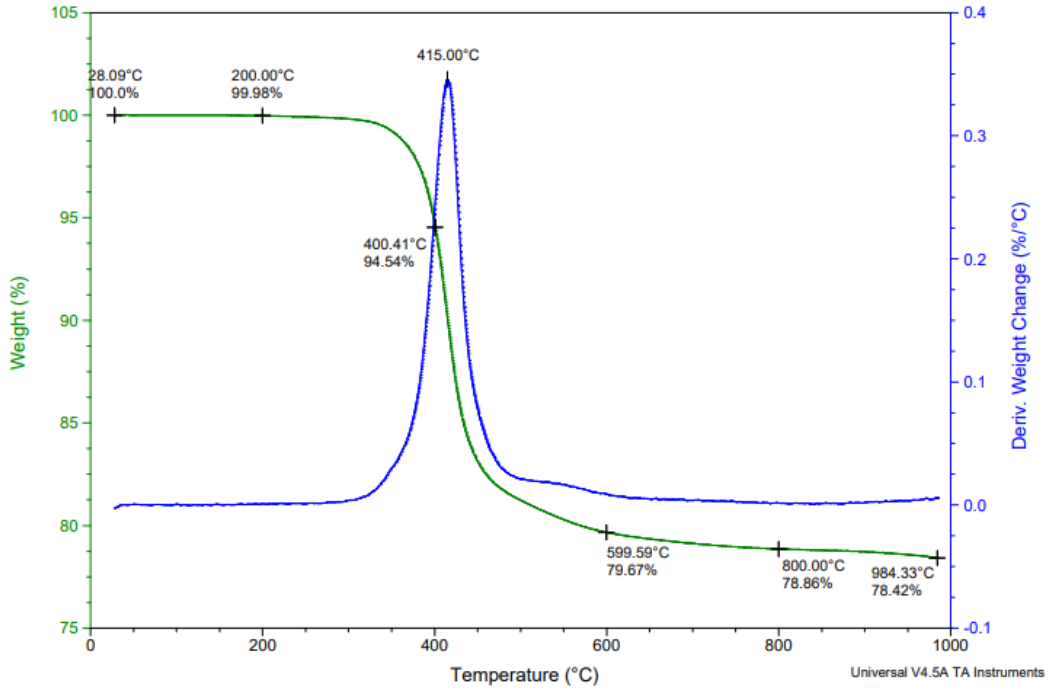

Figure S.30. TGA plot of Z3-1 measured in a nitrogen atmosphere.

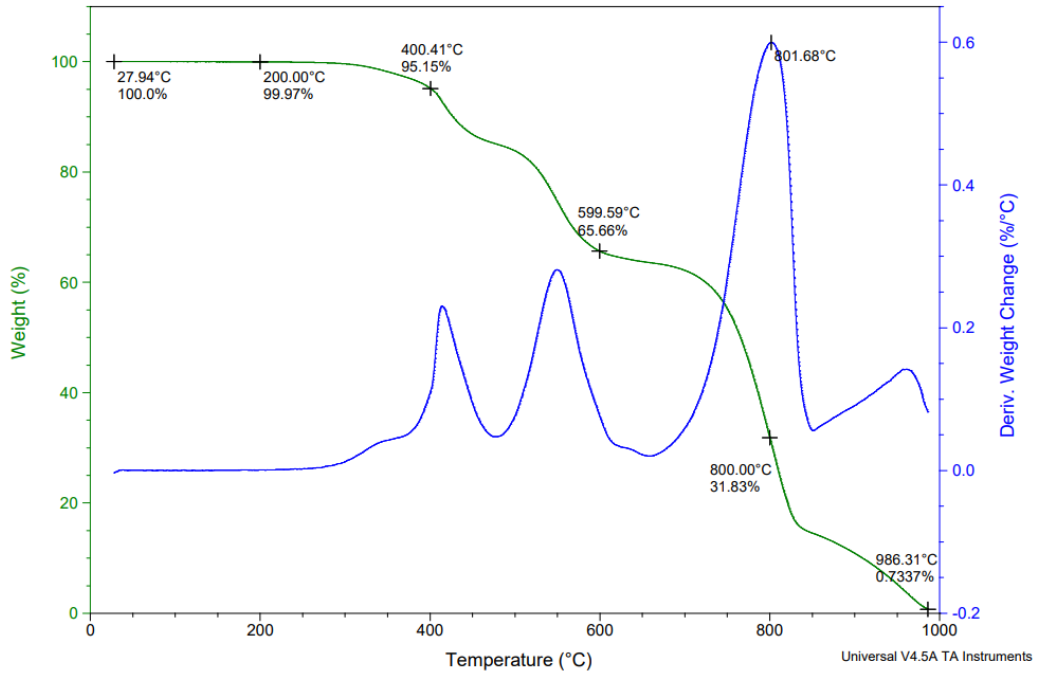

Figure S.31. TGA plot of Z3-2 measured in an air atmosphere.

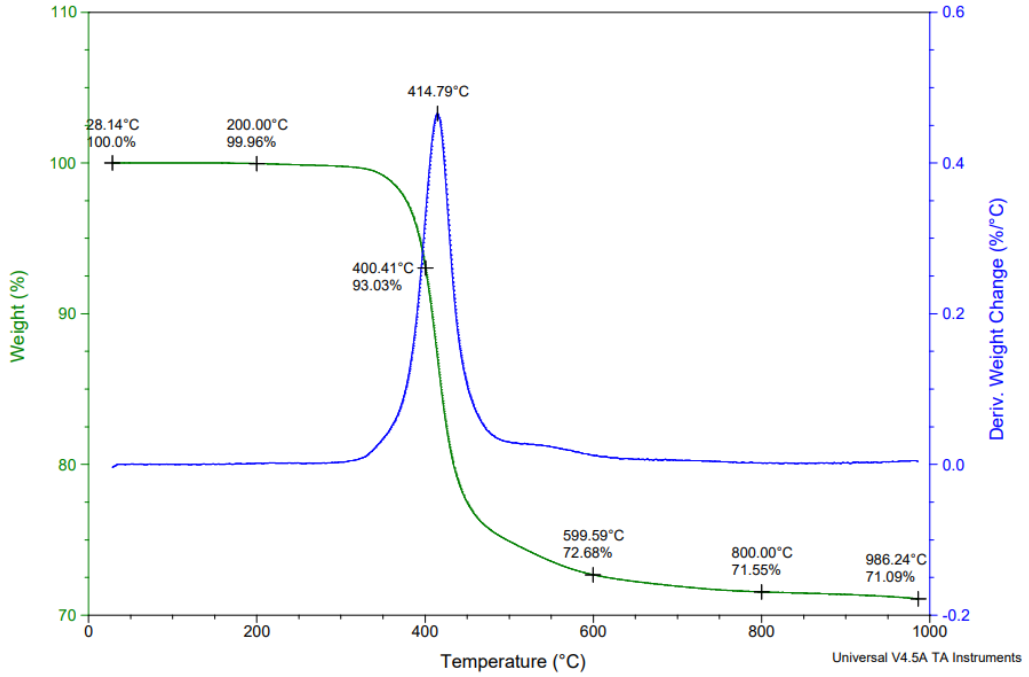

Figure S.32. TGA plot of Z3-2 measured in a nitrogen atmosphere.

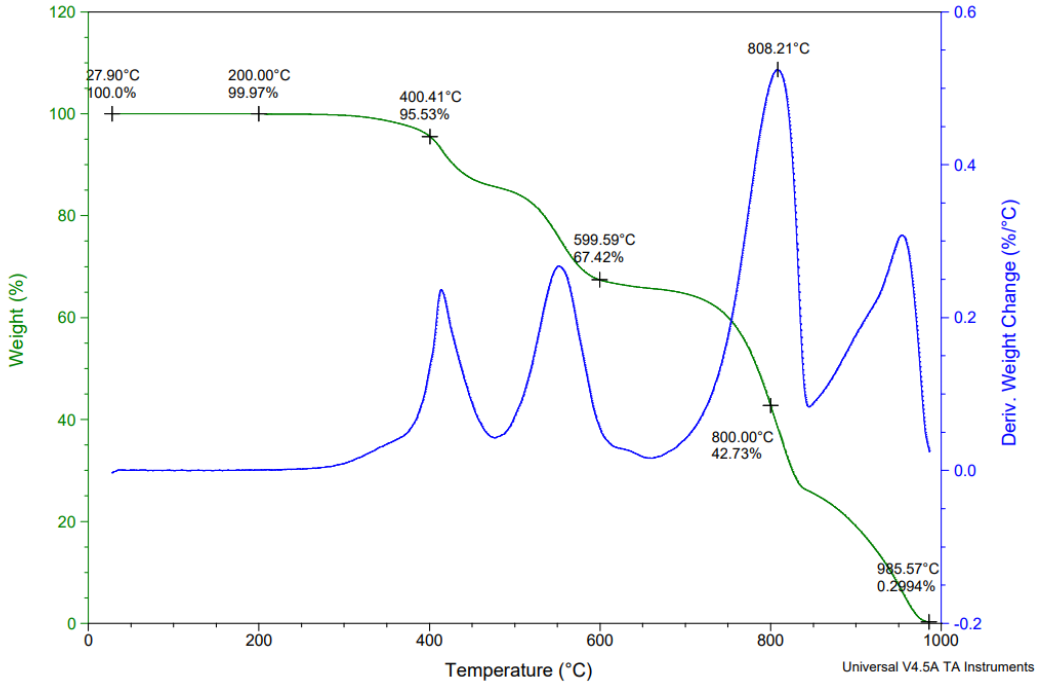

Figure S.33. TGA plot of Z4-1 measured in an air atmosphere.

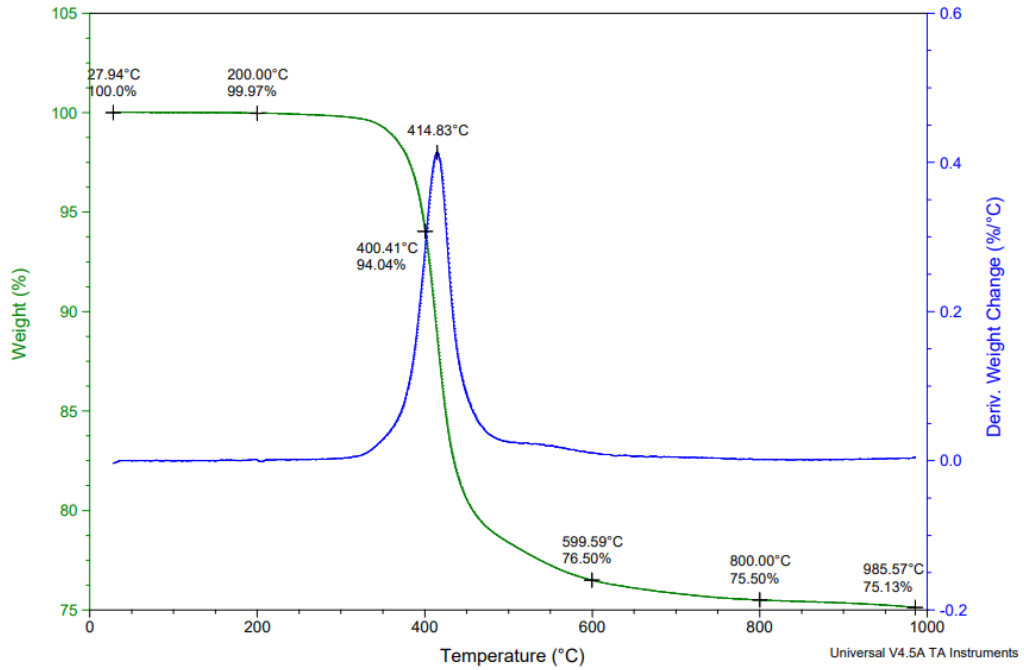

Figure S.34. TGA plot of Z4-1 measured in a nitrogen atmosphere.

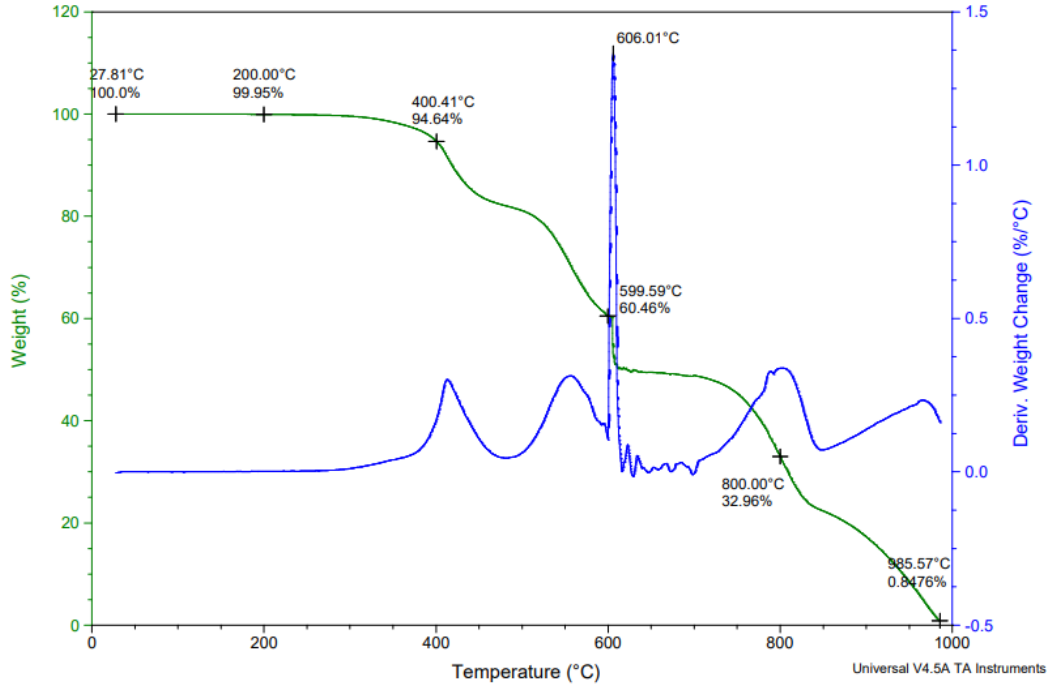

Figure S.35. TGA plot of Z4-2 measured in an air atmosphere.

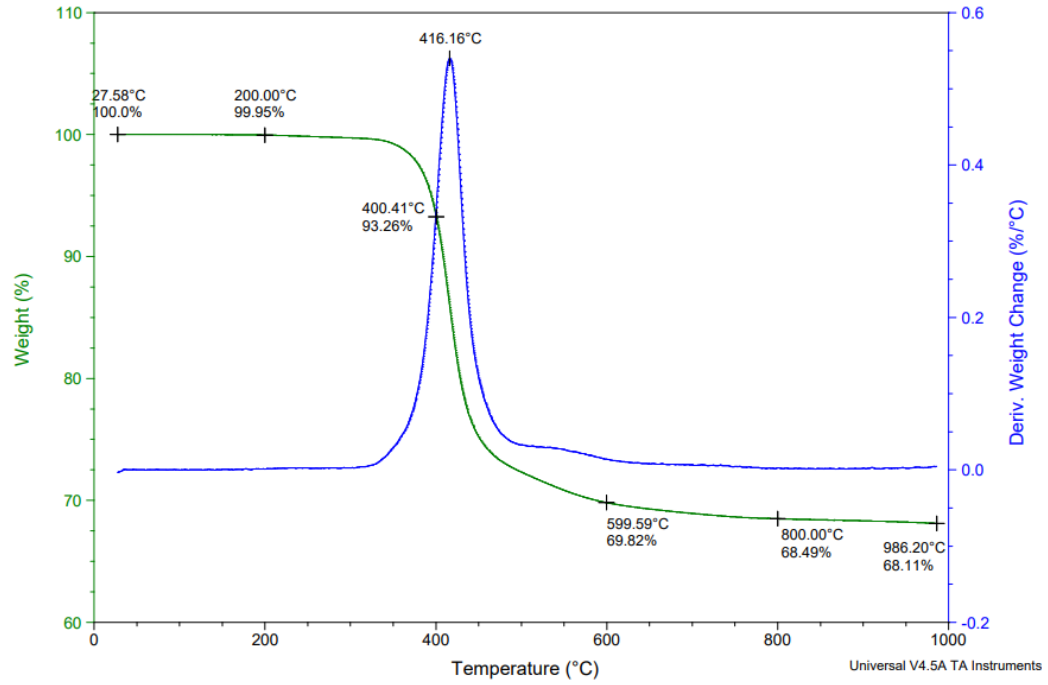

Figure S.36. TGA plot of Z4-2 measured in a nitrogen atmosphere.

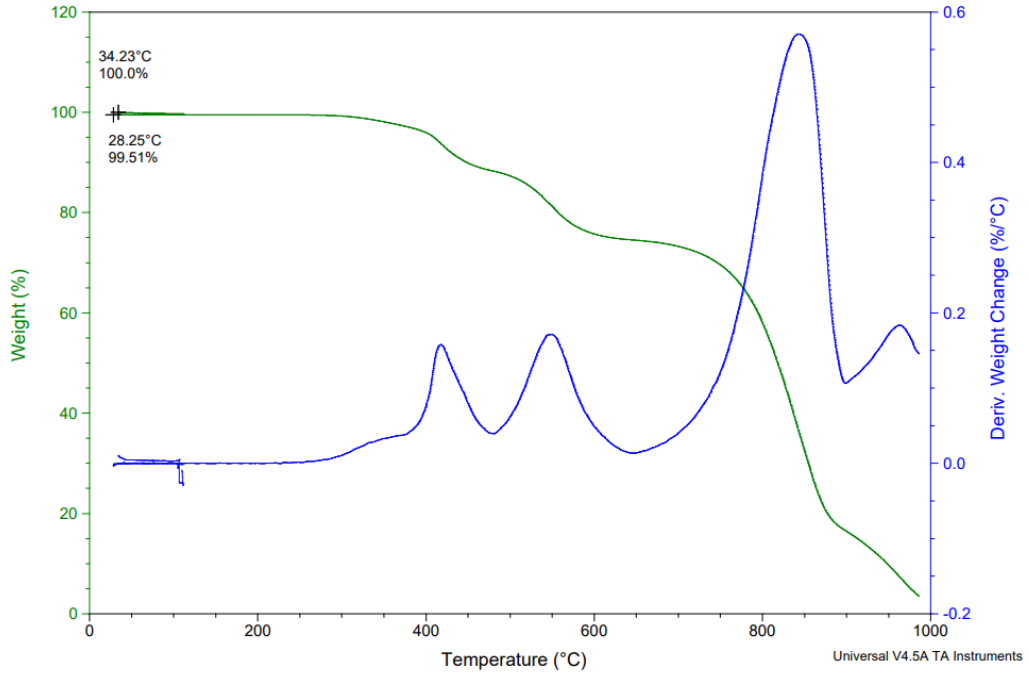

Figure S.37. TGA moisture loss plot of Z2-1 measured in an air atmosphere.

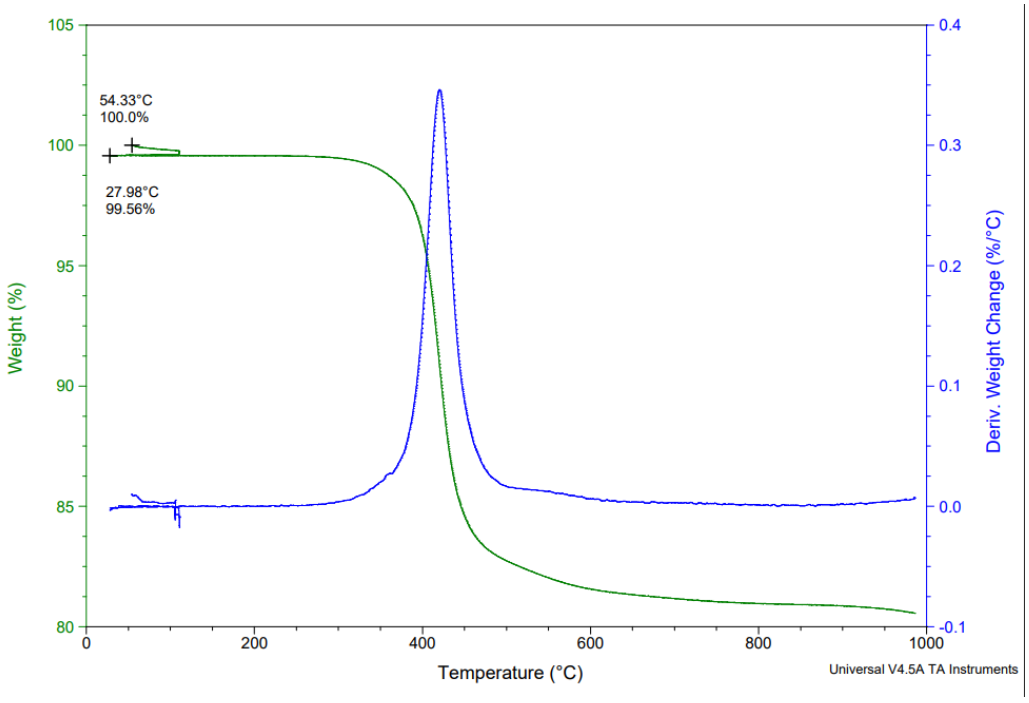

Figure S.38. TGA moisture loss plot of Z2-1 measured in a nitrogen atmosphere.

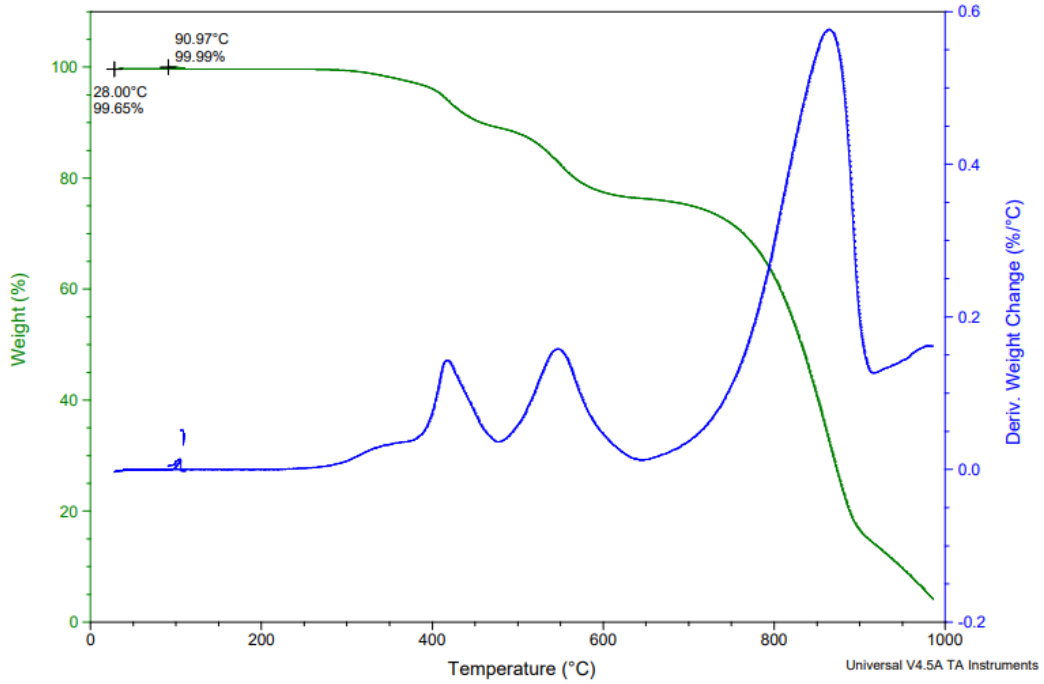

Figure S.39. TGA moisture loss plot of Z2-2 measured in an air atmosphere.

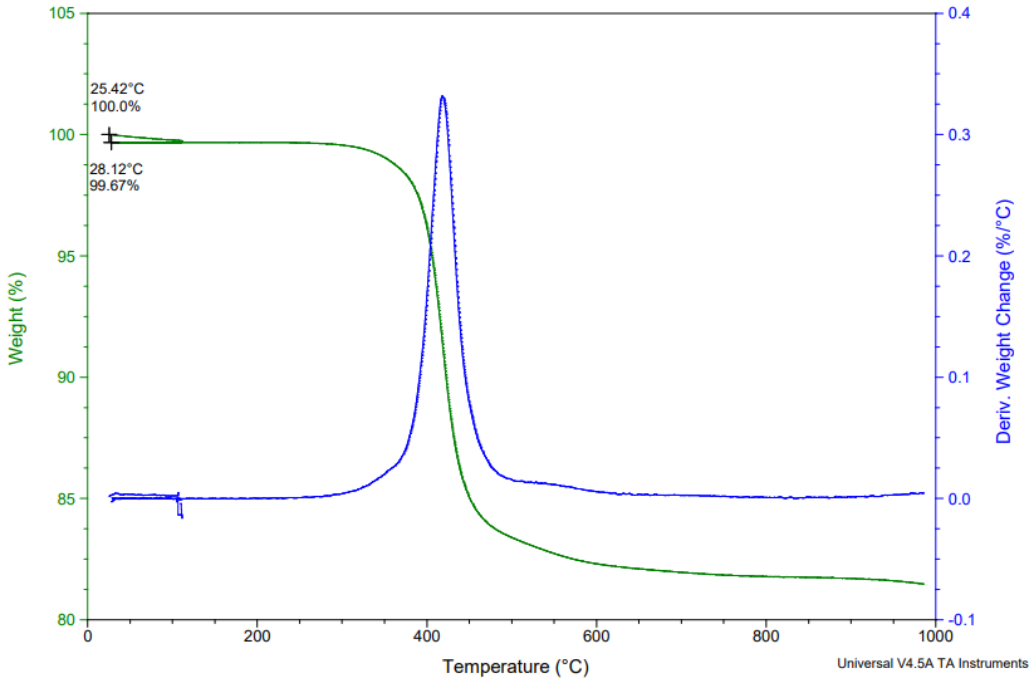

Figure S.40. TGA moisture loss plot of Z2-2 measured in a nitrogen atmosphere.

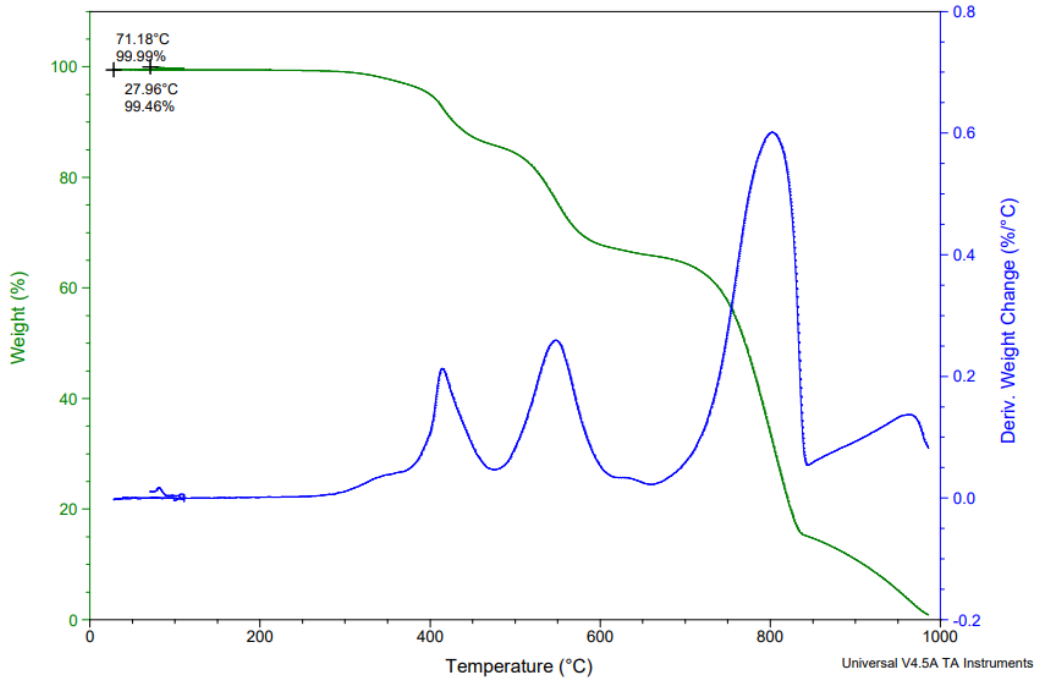

Figure S.41. TGA moisture loss plot of Z3-1 measured in an air atmosphere.

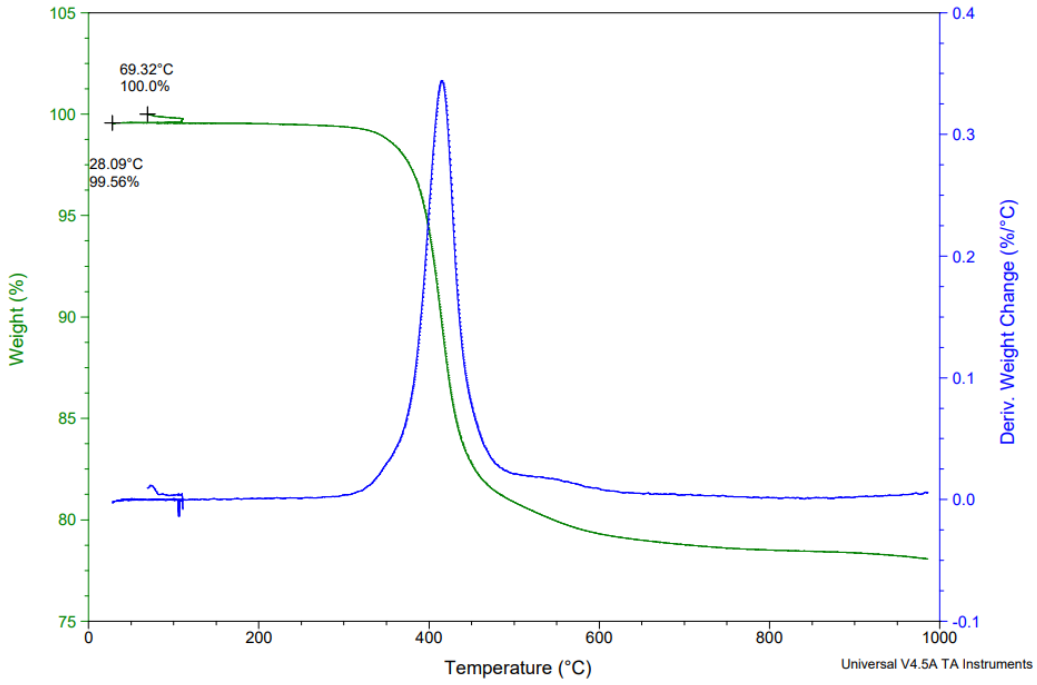

Figure S.42. TGA moisture loss plot of Z3-1 measured in a nitrogen atmosphere.

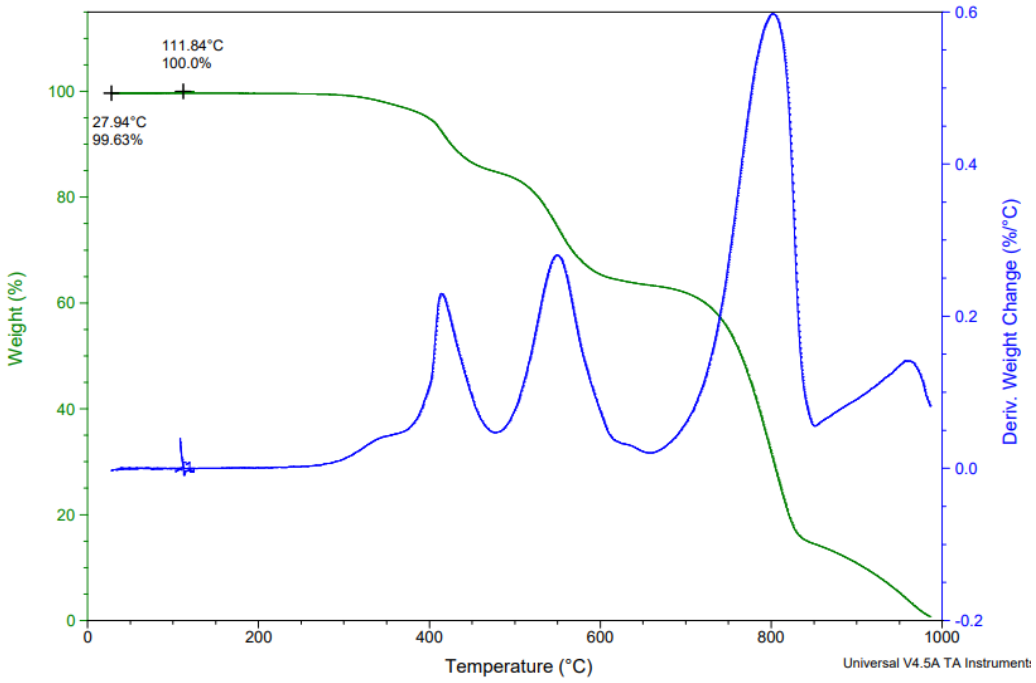

Figure S.43. TGA moisture loss plot of Z3-2 measured in an air atmosphere.

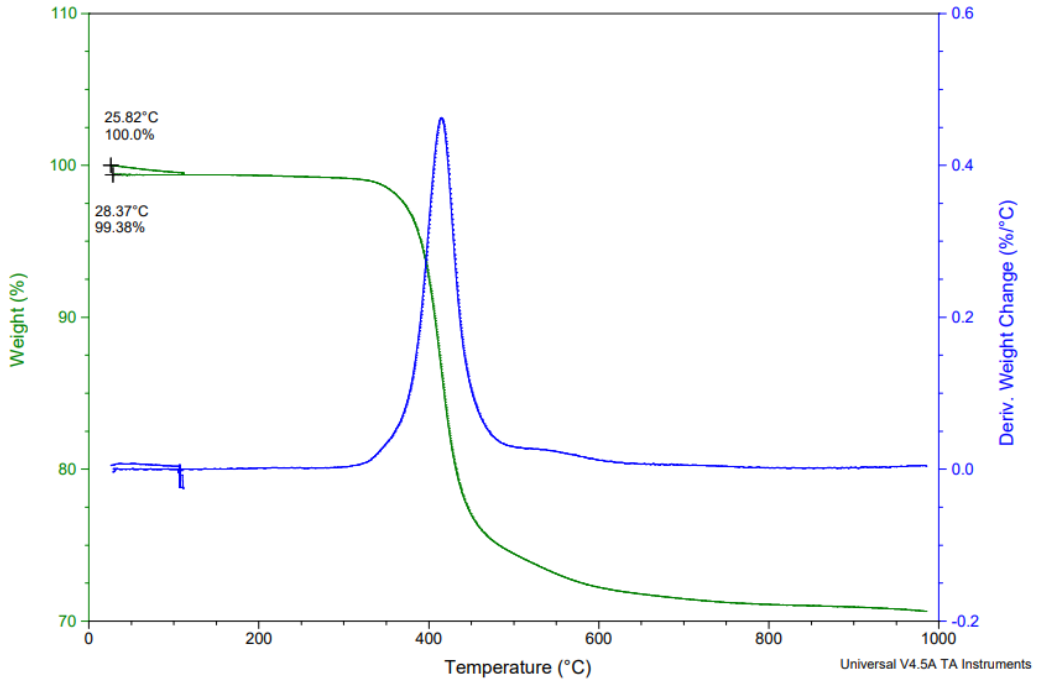

Figure S.44. TGA moisture loss plot of Z3-2 measured in a nitrogen atmosphere.

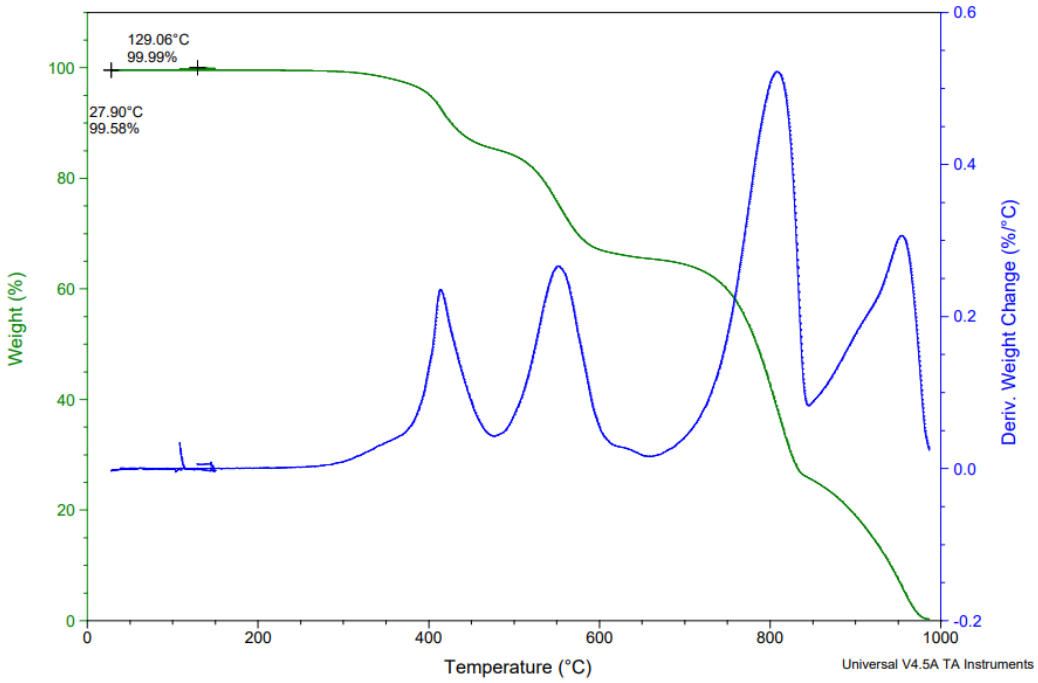

Figure S.45. TGA moisture loss plot of Z4-1 measured in an air atmosphere.

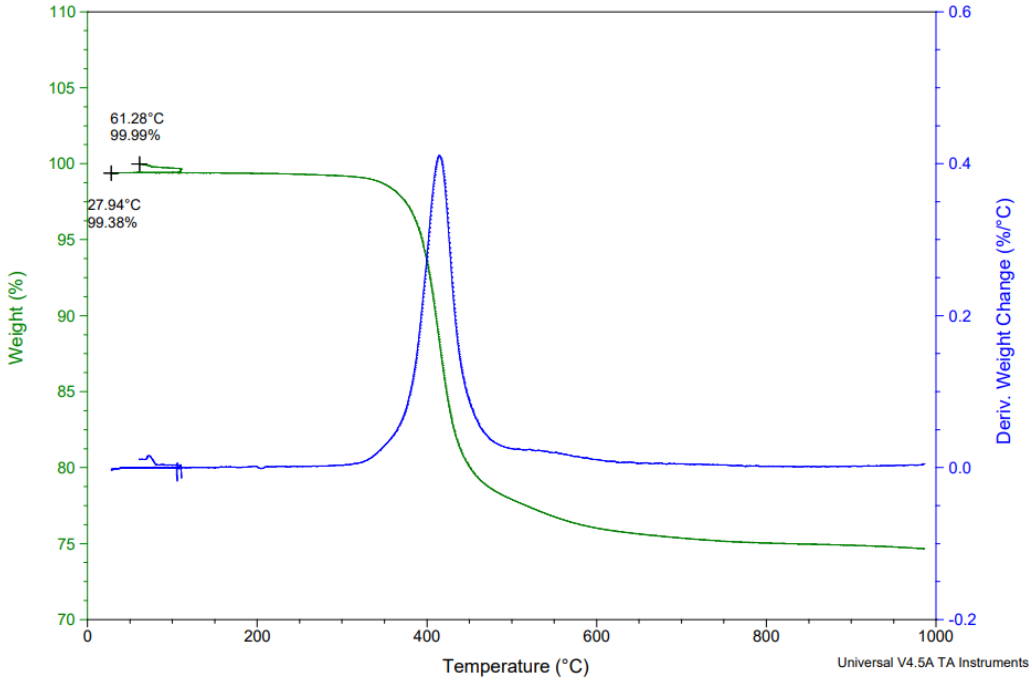

Figure S.46. TGA moisture loss plot of Z4-1 measured in a nitrogen atmosphere.

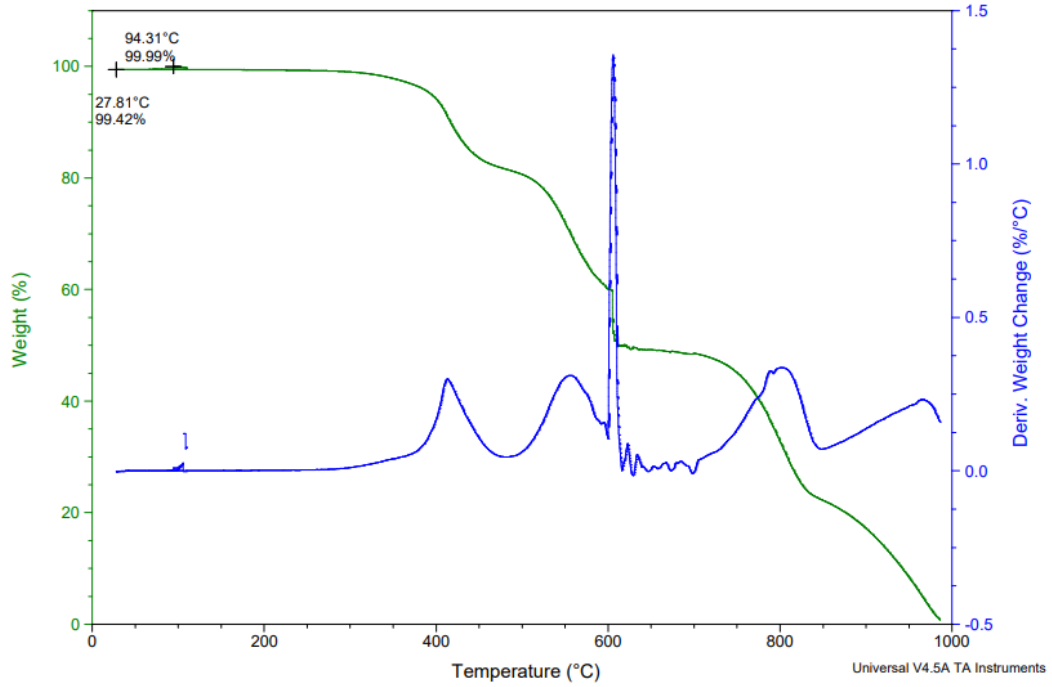

Figure S.47. TGA moisture loss plot of Z4-2 measured in an air atmosphere.

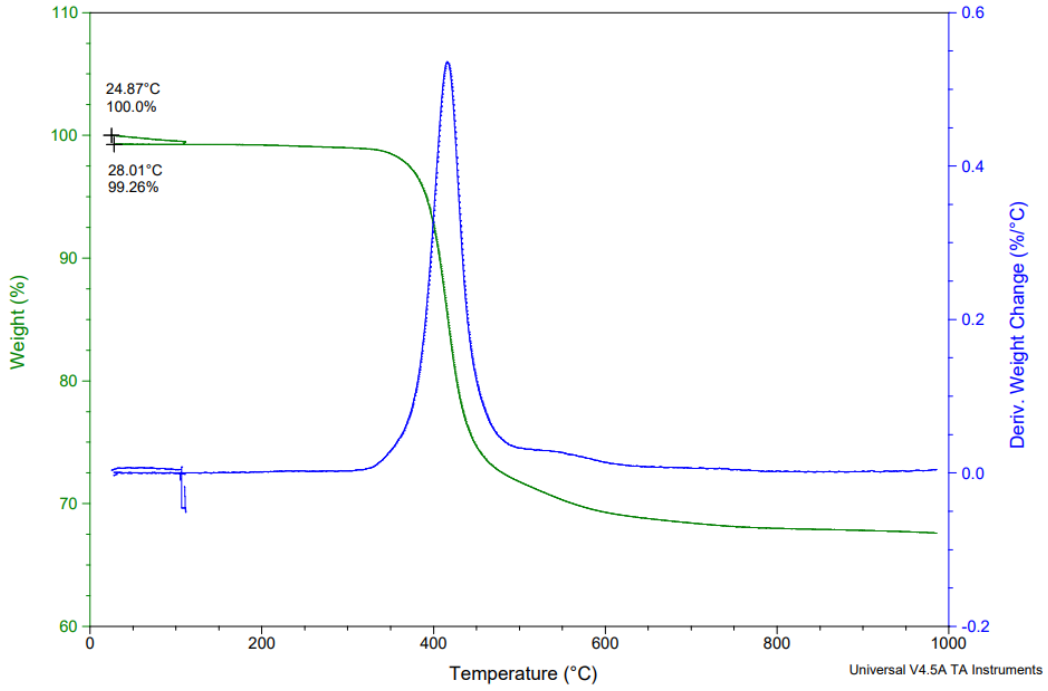

Figure S.48. TGA moisture loss plot of Z4-2 measured in a nitrogen atmosphere.